1-1-2018

NANOTECHNOLOGY-BASED CANCER PHOTOTHERAPY AND CIRCULATING TUMOR CELL ANALYSIS

Ryan Timothy O'Connor

NANOTECHNOLOGY-BASED CANCER PHOTOTHERAPY AND CIRCULATING TUMOR CELL ANALYSIS

By

Ryan Timothy O'Connor

A Dissertation

Submitted in Partial Fulfilment of the

Requirements for the Degree of

Doctor of Philosophy

Major: Chemistry

The University of Memphis

December 2018

Acknowledgements

First, I would like to thank Dr. Xiaohua Huang. Her guidance and support even through times when I thought I could not continue has been an immeasurable act of patience and dedication that has made this all possible. I would also like to express thanks to Dr. Yongmei Wang for her perpetual support and optimism. Additional thanks go to Dr. Gary Emmert for his leadership and mentoring.

Second, I would like to thank my group members past and present, most notably Dr. Saheel Bhana, Dr. Elise Chaffin, Elyahb Allie Kwizera, and Ray Wilson, for their exceptional work on these projects and invaluable friendship. I also thank the graduate student corps of the Chemistry Department.

Finally, I thank my loving wife Kaylee for her perpetual support throughout the last half-decade, and my dog Oura, who sat next to me throughout the writing of this document.

Preface

This dissertation includes material from three journal articles, two of which are published at the time of this writing. The literature review incorporates material adapted from "Gold Nanoparticle Based Platforms for Circulating Cancer Marker Detection", which was published in Nanotheranostics. It was adapted with permission from (Huang, X., O'Connor, R. T., Kwizera, E. A. "Gold Nanoparticle-based Platforms for Circulating Cancer Marker Detection" *Nanotheranostics* **2017** *1(1),* 80-102) Copyright 2018 Ivyspring International Publisher.

Chapter 4 is based upon the paper "Photosensitizer-loaded Gold Nanorods for Near Infrared Photodynamic and Photothermal Cancer Therapy", which was published in the Journal of Colloid Interface Science. It was adapted with permission from (Bhana, S., O'Connor, R. T., Johnson, J., Ziebarth, J. D., Henderson, L., and X. Huang. "Photosensitizer-loaded Gold Nanorods for Near-Infrared Photodynamic and Photothermal Cancer Therapy" *J. Coll. Int. Sci.* **2016** *469*, 8-16) Copyright 2016 Elsevier, inc.

Chapter 5 is based upon the paper "Isolation, Detection, and Analysis of Circulating Tumor Cells Using Iron Oxide-gold Core-shell Nanoparticles" which is currently in preparation by the authors.

Abstract

Ryan Timothy O'Connor. The University of Memphis. December 2018. Nanoparticle-based Phototherapy and Circulating Tumor Cell Analysis. Major Professor: Xiaohua Huang, Ph.D.

Gold and hybrid gold nanotechnology are uniquely poised to improve the fields of cancer diagnosis and therapy. Modifying gold nanoparticles with biological proteins has been widely used for decades, however, the common carbodiimide technique requires steps that reduce sensitivity and effectiveness in some spectroscopic techniques. We have developed an antibody conjugation protocol which conducts linking first, and then covalently adheres the antibody-linker complex to the nanoparticle surface. The linking polymer N-hydroxysuccinimide-polyethylene glycol-thiol (NHS-PEG-SH) was incubated with a protein overnight and purified by centrifuge filtration before modifying the surface of gold nanoparticles by slow mixing. The method was transferred to antibody conjugation and cell-labeling strength and specificity verified via dark field imaging of cell lines with known expressions. In cancer treatment, nanoparticles have been implemented in promising phototherapeutic strategies. Here, we describe the development of a nanocomplex which augments photothermal therapy via gold nanorods with the addition of a photosensitizer for dual photothermal-photodynamic (PTT/PDT) therapy under a single laser irradiation. Silicon 2,3-napthallocyanine dihydroxide (SiNC) was adsorbed onto gold nanorods and stabilized with alkylthiol-polyethylene glycol. Cytotoxicity was analyzed in vitro under laser treatment. It was found that the nanocomplex produced cell-killing effects with efficiency greater than PTT or PDT alone under low dosage and cell-killing efficiency increased with increasing alkylthiol length.

This nanocomplex has potential to non-invasively destroy tumor cells in a localized area, preventing tumor resurgence. In cancer detection, circulating tumor cells (CTCs) are the hallmark of metastasis and an ideal target for liquid biopsies but are exceptionally rare. Here we develop on the previous system by using multiplexed antibody-targeted SERS-active iron oxide-gold core-shell nanopopcorn in conjunction with a miniaturized chip to capture CTCs from whole blood and analyze individual cells to construct a molecular profile of common cancer markers. We demonstrate the capability of the nanoparticles to selectively capture and profile cancer cells individually and with multiplexed labeling with an integrated microfluidic device. Labeled cancer cells spiked into PBS are swiftly captured with high efficiency, and detected nanoparticle ratios agree with cell line expressions. This method provides a rapid integrated method for CTC capture, detection, and profiling of surface markers.

TABLE OF CONTENTS

List of Figures

Chapter 1

Introduction

Nanotechnology is broadly classified as the development of devices and technology with materials whose scale ranges between 1 and 100 nanometers in some characteristic. This size range yields unique properties that bridge bulk materials and individual molecules and is often distinct from both. The control and manipulation of materials to create nano-scale structures requires rigorous synthetic design and control to achieve the desired properties, and precise instrumentation to verify these properties. Nanotechnology has been a target for considerable scientific research for over fifty years[1]. In that same span, research behind finding uses for these particles has blossomed into a wide range of applications confronting the most pressing issues of the modern day[1,2 3]: energy production and storage, engineering[4], efficient and safe chemical catalysis[5,6,] and medicine[1,7,8,9]. In the latter case, nano-scale materials provide a unique interface at similar scales to biochemical components and allow for designs that directly influence the human body on a cellular level[10]. As such, nanotechnology is not an individual field of science but a meeting point of various disciplines, including physics, materials science, chemistry, and biology.

Cancer remains the second most common cause of death in the United States with over 590,000 victims in 2015[11]. While our understanding of the disease and the available treatment options have vastly improved in the last ten years, the disease remains a significant challenge to human life. The advancement of nanotechnology has opened new avenues in early cancer detection and treatment and development has grown exponentially in the last twenty years[1,3]. The near-infinite multitude of variation in

nanoparticle implementation also presents a similarly wide-ranging array of challenges which must be explored to build more advanced and functional nanotechnology.

In the field of cancer medicine, two fields have seen direct advancement with the introduction of nanotechnological platforms[1]. The first is in the field of non-invasive treatment, in which the small size and high functionality of nanoparticles allows for alternatives to more risky treatment options or augments other treatments to improve patient prognosis. The second field is that of early cancer detection and diagnosis, in which patient survivability is improved by the more accurate early warning of the presence of cancer, problems arising from treatment, or changes in disease characteristics.

This work focuses on developing gold and iron oxide-gold core-shell nanoparticles for both fields by utilizing the unique properties that arise from nano-scale gold. First, this research aims to provide a simple and adaptable bioconjugation technique for use in broad research strategies. Second, this research aims to further the development novel phototherapy vehicles for non-invasive cancer treatment. Third, this research aims to push forward the concept a one-step SERS-based CTC detection strategy towards clinical relevance and potential implementation.

Overview of Chapter Contents

Chapter 2 presents the literature review, which broadly describes the genesis of modern gold nanoparticle synthesis and the relevant physical and optical properties that exist with these substances. Additionally, functionalization and core-shell structures are discussed. Secondly, nanotechnological applications related to non-invasive cancer treatment and cancer detection and prognosis are explored. In Chapter 3, we explore the

development of a specialized method of protein conjugation to gold nanoparticles and gold-shell nanoparticles which will minimize the detrimental effects observed in previous studies. In Chapter 4, we discuss the development of a nanocomplex constructed around gold nanorods which is capable of simultaneous photothermal and photodynamic therapy of cancer cells. In Chapter 5, we discuss the development of a more advanced circulating tumor cell detection method in which iron oxide-gold core-shell nanoparticles are used for magnetic capture followed by multiplexed detection and molecular profiling of cancer cells in whole blood. Finally, a summary of conclusions brings together the main ideas of each chapter and presents recommendations of continuing studies.

Chapter 2

LITERATURE OVERVIEW

From Gold Nanoparticle Discovery to Overcoming Challenges in Cancer Treatment with Gold Nanotechnology

Gold Nanoparticle Synthesis Overview

Gold in its nanoparticle form has been manufactured for thousands of years, particularly to exploit its optical properties as a method of staining glass. The first scientific creation and study is generally accredited to Michael Faraday who, in 1856, made a ruby-red solution of colloidal gold while attempting to chemically mount gold to microscope slides. Faraday was able to discern that the coloration was indeed due to particles of gold too small to observe at the time, and not by some accidental synthesis of a new chemical compound[12].

While Faraday's accidental in-solution reduction of gold salt was a clear synthetic success, it was not until 1951 that John Turkevich developed a simple method produced a monodisperse population of gold nanoparticles between 10nm and 20nm through the reduction of chloroauric acid with trisodium citrate at near-boiling temperatures[13,14,15]. As extrapolated by Zurkowski *et al.*. and refined by Pong, *et al.*, in this reaction, the size and shape of the particle was not a result of random gold reduction, but kinetically determined by the two-stage process by which the nanoparticles are synthesized. The first stage, known as nucleation, is initialized by the genesis of a multi-coordinated system of auric acid and oxidized trisodium citrate that was recently discovered to collapse into an extensive network of thin wire-like filaments in solution[16]. The wires, formed rapidly and with many different crystalline orientations, widen and eventually break up into segments

from repulsion forces. The solution color changes from the faint yellow of chloroauric acid to a light grey color as the nanowire network is formed, and finally a transition to a reddish color as gold nanoparticles separate. This reaction does not consume the entirety of either chloroauric acid or sodium citrate in solution, but the final size of the synthesized nanoparticles is heavily reliant on the relative concentrations of starting material[16,17]. Particles larger than 20nm had wide size ranges, and thus were not ideal synthetic products of this method.

The Turkevich method was succeeded by a wide range of alternatives to generate gold nanoparticles under different conditions to mitigate the limitations of this original procedure. The Brust-Shiffrin method, for example, produces highly monodisperse nanoparticles in the organic phase by sodium borohydride reduction and phase-transfer mediation by tetraoctyl ammonium bromide, followed by dodecanethiol stabilization[18]. The disadvantage of this method lies in the thiol-based stabilization, which reduces the potential modification options, though Murray *et al.*, managed to address this[19,20]. Highly monodisperse populations were made from ultrasonic stimulation of a solution of chloroauric acid and a capping agent, whereby the reduction is carried out by hydroxyl radicals formed by the induced cavitation[21]. Schmid's cluster produces a unique gold nanoparticle in that the particle is created as a true molecule with precisely 55 atoms of gold connected and stabilized by phosphine[22]. Contemporary methods typically employ the use of sodium borohydride as the reducing agent due to its rapid action at room temperature[23,24,25]. The varying component in many synthetic methods is the capping ligand, with examples such as 4-(N,N-dimethylamino)pyridine, tetraoctoammonium bromide, cetyltrimethylammonium bromide and chloride, and others[26].

The creation of different shapes and morphologies has a wide range of uses in the application of nanoparticles to other fields. Many of these syntheses take place in water and rely on a technique known as the seed-mediated growth method. Seed-mediated growth is an exploitation of the two-step nanoparticle synthesis process first hypothesized by Turkevich *et al*. Nucleation requires rapid reduction in solutions at relatively high concentrations, leading to small spherical particles. Non-spherical particles are difficult to produce, as nucleation is less likely to occur under the necessary conditions, especially lower concentration of gold ions and a slower reduction process. Seed-mediated growth physically separates these two methods entirely. The 'seed' particles are synthesized under rapid conditions and high concentration to produce individual nanoparticles of spherical shape and small size. The 'growth' stage is then undertaken by altering the reaction to utilize a new reductant, gentler reaction conditions, and more gold[1,26].

The most well-understood anisotropic gold nanoparticle is the gold nanorod, a cylindrical nanostructure with rounded ends. First developed by Catherine Murphy's group, gold nanorods are grown from 2-5nm seeds produced via the Turkevich method. These seeds are then injected into a growth solution containing chloroauric acid, ascorbic acid, and cetyltrimethylammonium bromide (CTAB) stabilizing agent. Ascorbic acid reduces gold in solution from a 3+ oxidation state to 1+, then gold is further reduced by surface catalysis on the seed, inducing growth of the particle[27]. Early anisotropy develops by a slightly selective preference of Au+ ions to deposit at a specific crystal structure facing ({100} specifically) which results in initial uneven particle growth[28]. CTAB micelles possess a highly positive charge and as such greatly reduce the rate at which positively-charged ions travel through the bilayer. For the sides of an anisotropic

particle, CTAB is tightly-packed and deposition occurs at a very slow pace. On the ends, however, high curvature of the nanoparticle spreads the micelle spacing and allows more rapid ion deposition on the surface, thus facilitating the rapid lengthening of the particle on select faces[29,30].

With careful tuning of reaction conditions, size and aspect ratio could be varied from nearly 1 to 6 with yields up to 50%. This dampened yield was discovered to be the result of the seed particle formation, which readily forms a five-fold crystal twinning pattern that facilitates growth on only one axis[31]. Yield and aspect ratio control increased when silver nitrate was incorporated into the growth solution, which allows for underpotential deposition (the deposition of a "less-noble metal" on a cathodic metal surface, forming a thin film, at potentials under that which would normally be required for the atoms in question) of silver onto the surface of the gold seed. Strong binding of silver on certain gold crystal faces ({110} specifically) inhibits the deposition of gold on these faces. Combined with CTAB control which facilitates ion deposition on the 'ends' of an anisotropic object, nanorod growth is promoted along a single axis, less-favored by silver and porous to the influx of gold nanoparticles[32].

This complication is eliminated entirely by using seeds produced when reducing chloroauric acid with sodium borohydride in a CTAB solution. The seeds created in this method are in the 1-3nm range, as compared to the 4-5nm range before and, more importantly, are of a single crystal structure with no mirror planes. El-Sayed and Nikoobakht groups first produced gold nanorods from these single-crystal seeds with exceptional yield. Inclusion of carefully-measured concentrations of silver ions can

produce a range of aspect ratios from 1.5 to 5 with yields near 99%[33]. This procedure has since become the most common synthesis method for nanorods[26].

Significant modification of the gold nanorod synthetic method, especially in silver ion and capping agent concentration, unlocks a wide range of shapes of gold nanoparticles. For example, polygonal, angular shapes with four to ten sides are synthesizable in narrow ranges of concentration of both reactant parameters, indicating the influence of both in guided shape growth. Low CTAB concentrations correlate with fast deposition of gold atoms on specific crystalline faces, while the inverse favors more even distribution between faces. 'Plates' or flat particles with a geometric edge, are also available with significant growth solution modification, first in pH through the addition of NaOH, and later in the adoption of alternate stabilizing or reducing agents. Considerably more complex gold nanoparticles (multi-lobed particles, nanowires, etc) have been synthesized with great difficulty, and at low yield[1,26].

Paramount Gold Nanoparticle Properties

Scientific interest in gold nanoparticle synthesis has been fueled by the multitude of exceptional qualities these particle exhibit, utterly unlike atomic gold or bulk gold formations[1,2]. Like all nanomaterials, gold nanoparticles possess a high surface area for their volume, allowing for efficient interactions with nano-scale targets. Unlike other platforms, gold nanoparticles are easy to synthesize, simple to functionalize, quick to be made biocompatible, and exhibit extraordinary optical properties due to the presence of a localized surface plasmon resonance (LSPR)[34]. LSPR is a phenomenon that arises from the collective oscillation of conduction-band electrons around metal nanoparticles induced by the electric field of incident light. As a result, nanoscale metals very strongly

absorb light at the resonant frequency and the particle's localized electric field is greatly enhanced. Because the resonance occurs across the entire nanoparticle, its resonant wavelength, and therefore optical properties, is highly dependent on the particle's shape, size, material, and dielectric constant[35].

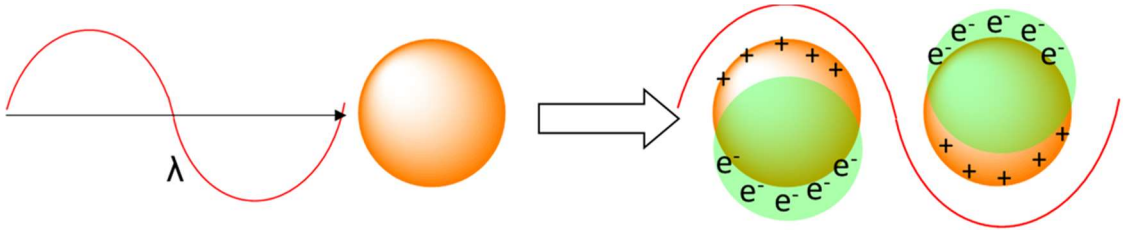

Figure 2.1: Schematic representation of light interacting with a gold nanoparticle to produce localized surface plasmon resonance.

Light that is absorbed by metal nanoparticles is either scattered at its original wavelength or the heightened electronic state will impart some energy into the particle itself through the generation of a phonon, or phased lattice vibration. Phonon energy that exceeds the lattice energy can induce melting of the particle, while energies imparted that vastly exceed lattice energy result in ablation. In all cases, the particle temperature increases when exposed to light at or near their resonant wavelength, but the material identity determines which mode is the dominant relaxation pathway[36,37].

In addition to producing exceptional scattering and heating effects, nanoparticles' optical properties give rise to other spectroscopic effects. Two major examples are their influence on fluorescence and Raman scattering. Fluorescence is an electronic-photonic phenomenon in which incident light of a specific energy state is absorbed by a fluorescent molecule, which excites an electron to a higher energy state. The electron then relaxes through a series of vibrational changes until collapsing back into a low-energy state and emitting a new, lower-energy photon. This emitted photon is typically of

a color well-separated from the initial source and can be observed independently of the incident light using a pass filter. Except for some fluorescent tools such as quantum dots, fluorescent compounds are susceptible to photobleaching and interference effects.

Fluorescence is enhanced by proximity to an appropriately-plasmonic nanoparticle as the scattered photons from the particle locally increase the incoming light[37]. The result is an effective increase in quantum yield of the fluorescent molecules, however this is highly dependent on nanoparticle size and shape. Metal nanoparticles whose plasmon resonance is heavily weighted towards absorption effects do not significantly enhance fluorescence in nearby molecules, whereas particles irradiated with wavelengths of light that strongly favor scattering (either by tuning nanoparticle morphology or irradiation wavelength) will produce enhanced fluorescent effects[38,39].

Light that impacts a molecule which possesses sufficient degrees of freedom can be absorbed to induce a polarization of the molecule. Typically, these molecules relax and re-emit a photon of identical energy to the incident light, in a random direction. Certain molecules with vibrational or rotational modes that resonate with this induced polarization will rarely produce a coupling effect that changes the energy of the emitted photon upon relaxation. The first case is an elastic scattering phenomenon called Rayleigh scattering, while the latter is known as Raman scattering. Both involve an excitation to a virtual energy state that immediately collapses to either the same energy level as before (Rayleigh scattering) or a different level that results in Raman scattering. The photon energy change (or 'shift') results in either a higher molecular energy state and photon energy loss, known as a Stokes shift, or a lower molecular energy state and photon energy gain, called an Anti-Stokes shift. At most experimental temperatures,

most electrons exist at ground or near-ground state, thus Stokes scattering is far more common. However, Rayleigh scattering is significantly more common than either; of every ten million photons that are scattered by a material, only one will scatter inelastically. This rarity limits the ability to utilize Raman scattering, however there are some distinct characteristics that are exploitable and even advantageous when compared to other phenomena such as fluorescence. First, Raman spectroscopy is heavily reliant on the vibrational modes of the active molecule and thus exclusive to that molecule's identity. When measured on a spectrometer, the result is sharp, fingerprint spectra between 10 and 100 times sharper than peaks yielded by fluorescence molecules. Second, Raman scattering is not affected by autofluorescence of biological materials or traditional photobleaching effects. Third, Raman scattering does not require electronic excitation to an explicit 'stationary' state to occur, therefore scattering is observed regardless of incident wavelength, albeit at varying strength[40].

Raman scattering that occurs near a plasmonic surface has a special name: surface-enhanced Raman spectroscopy (SERS). Two mechanisms apply to explain this phenomenon: chemical and electromagnetic enhancement. Chemical enhancement is described as the result of charge-transfer effects in which plasmonic electron motion provides an alternate pathway with which electrons elevate to a virtual excited state. Electromagnetic enhancement results from the boosted electromagnetic field in which the oscillating electrons further augment the field applied by incident light[41]. This is described in the equation for field enhancement A(ν) below

1) $$A(\nu) = \frac{E_M(\nu)}{E_0(\nu)}$$

where $E_M(\nu)$ represents the particle's electromagnetic field near the surface, and $E_0(\nu)$ is the incident light electric field. It is this E_M that is subject to enhancement by the LSPR. The result of field enhancement on SERS intensity ISERS is given below

$$2) \qquad I_{SERS} \sim |A(n_L)|^2 |A(n_S)|^2$$

where $A(n_L)$ is the field enhancement effect of the incident light and $A(n_S)$ is the field enhancement effect of the scattered light. In effect, SERS intensity is enhanced by E^4 relative to free Raman-active molecules. There are a few key traits of a nanoparticle that can be modified to increase this local electric field, such as the evolution of anisotropic nanoparticles, high-curvature regions, and aggregate solutions[40]. When this plasmon is localized, this electromagnetic enhancement mechanism is the most significant contributor towards Raman enhancement. Additionally, as in fluorescence, scattered photons from the nanoparticle effectively increase the optical cross section of Raman-active molecules near the particle[39,40].

The effect of this enhancement can increase Raman signal strength from 10^9 to 10^{14}, even resolving single molecule spectra as demonstrated by Nie *et al.*[42] and Kneipp, *et al.*[43]. Like fluorescence enhancement, nanoparticle size and shape tuning is necessary to produce an enhanced localized electric field without the majority of incoming photons being absorbed by the particle.

Multiplex targeting capability, rising from the fingerprint characteristics of Raman-active molecules and narrow peaks inherent of Raman scattering, allows for SERS NPs to provide greater volumes of information from a single irradiation. A SERS spectrum gathered from a mixture of different SERS NPs (i. e. those with different Raman-active dyes) produces a unified spectrum of all four dyes in a linear combination.

Each peak position represents one of the present dye molecules while intensity relates to concentration. With careful peak selection, multiple dyes can be used for multicolor detection and analysis of a target.

Plasmonic Nanoparticle Applications

Many metal nanoparticles possess strong plasmonic properties. Silver nanoparticles are regularly considered to have the strongest optical properties, especially for SERS usage, however recent computational studies have shown that this is heavily dependent on the laser chosen for spectroscopic analysis. Gold holds several advantages over the alternative metals. First, gold is inherently stable: cobalt and silver oxidize readily and thus lose their purity and plasmonic properties. This stability is even more pronounced when considering biological implementations: gold is effectively inert over a certain size (~4nm) while silver and cobalt produce cytotoxic effects as they react. Additionally, gold is readily simple to functionalize with the use of a gold-thiol bond[44].

Metal nanoparticles provide a wide range of possible implementations. In the 1980s, it was found that composite particles, which incorporate different types of nanomaterials, could produce elevated effects or present dual functionality. Early efforts focused on semiconductor nanoparticle modification but quickly expanded into other fields. Numerous hybrid nanoparticles exist but perhaps the most widespread implementation is carried out using a core-shell geometric strategy. The principle is simple: wrap or coat an existing nanoparticle (or several nanoparticles in a ‘cluster’) in a layer of an alternate material that either amplifies the desired effect or introduces a new effect for dual functionality.

Core-shell nanoparticles utilizing gold have considerable uses in electronic applications, biomedical labeling and imaging, and catalysis. Given the optical properties and biocompatibility of nanoscale gold surfaces, coupling gold with other nanoparticles is done with the goal of imparting these properties or augmenting them. Silica is the most commonly paired material, either as a core or a shell structure. Silica shells have greater use as a protective and functional coating for inorganic nanoparticles that would otherwise be toxic or unstable in complex environments. For example, silver nanoparticles, which possess strong SERS properties, rapidly oxidize and can be cytotoxic, limiting their use in water-based and biological applications. Magnetic nanoparticles assembled from metals and composites including nickel, iron, and iron oxides gain a stable, functional surface and water solubility when coated with silica, and are used in biological applications such as immunomagnetic separation. Gold/silica core-shell nanoparticles are constructed with the specific purpose of finely tuning the gold plasmon, modified by the dielectric constant of the silica as opposed to solvent, polymers, or capping agent[45]. However, as magnetic behavior and plasmonic interaction is dampened by increased shell thickness, most commercial applications of the above use a simpler organic shell structure using a well-studied and controlled polymer to produce the same stability effect. These include commercial applications, such as Dynabeads (ThermoFisher Scientific) for fluorescence analysis, magnetically-activated cell sorting with antibody-linked MicroBeads (Miltenyi Biotech), or extremely small iron oxide nanoparticles for specific MRI applications[46].

Nanoparticle Functionalization and Bioconjugation

Conjugating gold nanoparticles is necessary to provide stability and functionality for their intended use. In biological applications, nearly all gold nanoparticle uses require some modification of the surface. This is even more critical for particles synthesized and capped with CTAB, which is cytotoxic. Generally, gold nanoparticle functionalization is broken into two groups, physical and chemical, based on the properties governing the attachment. Physical interaction relies on innate properties of the components and the gold nanoparticle surface. Ionic interactions, hydrophobic association, and similar effects dominate physical functionalization. For example, the use of electrostatically-adhered bovine serum albumin on gold nanoparticles has boosted particle lifetime and stability in bio-active solutions. Chemical interactions are differentiated by chemical bond formation between the particles and their functional group. These most commonly utilize polymers and chemical bonding to the gold surface via gold-thiol chemical interaction, a method commonly used for gold-anchored self-assembled monolayers. While there are a wide range of electrostatic and hydrophobic strategies, the gold-thiol bond is the keystone of the covalent functional capabilities of gold nanoparticles[47].

Many functionalization strategies have been implemented to improve particle stability, especially in biological applications. Common polymers for improving biocompatibility include polyethylene glycol (PEG), Chitosan, Polymethacrylic acid, and others. Polyethylene glycol typically provides the most favorable conditions as controllable production and wide range of potential functional groups allow for the most options[46].

Conjugation of gold nanoparticles with bioactive proteins such as antibodies is of extreme importance to the successful implementation of the technology in biological

fields[48]. The ability to carry proteins as a payload or explicitly target cell populations via antibody-antigen interaction boosts the mechanical and analytical use of the platform considerably. The successful binding of antibodies to gold surfaces, however, is challenging and requires careful consideration of the nanoparticle environment. Simple physical adsorption has been used in the past with success[49,50]. Through the interaction of negatively-charged gold surface (as produced with CTAB-capped synthetic methods) with positively-charged amine groups in proteins, simple nonspecific adherence can be achieved. Hydrophobic association as the particle surface provides a restoring force that keeps the proteins anchored to the particle surface. This method of adherence has been used for optical and diagnostic imaging of diseases with good effect. However, this noncovalent bonding technique is hindered by several major weaknesses. The first major weakness is a lack of control of the orientation of the adherent protein, which may block or degrade the active component which gives the protein use. Antibodies chosen for specific binding of the F_{ab} region to cell features may be bound such that these same regions are not effectively exposed. Other proteins' active sites may be hidden or close interaction with a particle surface may disrupt the protein geometry. Due to a reliance on surface charge, pH significantly impacts the effect of electrostatic interaction, and other proteins in biological environments may readily bind and replace the intended proteins. Finally, the method requires a high concentration of protein to appropriately coat the particle with enough viable sites[51].

These problems were circumvented by implementing chemical strategies to anchor proteins to the nanoparticle. The most straightforward attempts included the direct binding of an antibody's sulfur groups directly to the particle surface, however this did

nothing to alleviate many of the problems of prior methods. Instead progress was found in the use of linking molecules and mediators. Replacement of the standard capping agents with bifunctional molecules which covalently anchor to the surface (almost exclusively via gold-sulfur bonding) and present new functional groups on the surface dominates gold nanoparticle functionalization. While nanoparticle stability is often hampered by harsh reaction conditions, biological conjugation techniques rarely exceed these limits. As such, the choices for the protein-active side of the bifunctional molecule are wide-ranging, depending on the required reaction. In the context of protein attachment, carbodiimide linking reliably attaches proteins to linking molecules and is indeed the most common method used for antibody conjugation of gold surfaces[52,53].

Overview of Gold Nanoparticle Applications Related to Cancer Treatment

The needs for medical tools to detect and treat challenging diseases is a limitless necessity for innovation. No human disease attracts more attention than cancer; as such the research that has been devoted to finding ways to manipulate nanotechnology to aid in its study and defeat is considerable. Two fields are of particular interest: non-invasive treatment and early detection and diagnosis. These will be discussed in turn.

Non-Invasive Treatment. The most common method of treating cancer outside of surgery is the use of anti-cancer pharmaceuticals. These drugs, also called chemotherapy agents, typically target the processes that institute cell division, thus delaying or hampering tumor growth. These drugs frequently possess poor pharmacokinetics and require large dosages that induce harmful side effects, particularly to the fast-dividing cells of the bone marrow and stomach lining. In addition, the effectiveness of these drugs is inconsistent between patients. Targeting chemotherapy

agents with an antibody improves specificity and allows for treatment to continue in patients who would otherwise be too compromised, however only a few of these pairings have passed clinical trials[54].

Nanotechnology presents some opportunity to improve upon chemotherapeutics through improvement of drug delivery. The goal of this implementation is to improve upon standard intravenous techniques by increasing effective drug delivery to the target area and reducing toxicity of treatment. This must be done with a nanoparticle that is itself biocompatible and possesses good distribution characteristics. Drug delivery systems made of repurposed biomolecules are common and range from micro-RNA constructs to engineered viruses. Lipid and polymer nanoparticles attempt to build nanoparticles which possess biocompatible outer layers and stable interior structures for drug packaging. Inorganic nanoparticles are heavily functionalized, by comparison, to introduce biostable elements and carry the drug. These latter are chosen for other properties of the inorganic core[55], either as a targeting scheme (such as magnetic localization[56]), controlling drug release[57], or as an additional therapy vehicle[58].

Delivery of nanoparticles to the desired area is either targeted or untargeted. Nanoparticles without a target rely on the enhanced permeability and retention (EPR) effect, a labeling of the tendency of tumors to develop unstructured and leaky blood vessel areas that collect nanoparticles of certain size distributions naturally[59]. Typical targeting strategies involve functionalization of the particle surface with a biomolecule that will bind specifically to the target cells. This is often an antibody chosen for its specificity to the target, though aptamers and other surface marker ligands have been used. Additionally, magnetic nanoparticle transports can be used to concentrate on a

specific area by applying a magnet to the desired location. Circulating magnetic nanoparticle particles that travel through the area of interest are held in place by the magnetic field, where the drug is released over time. This method, as a non-invasive treatment option, is limited to targeted areas that can be reached by a sufficiently powerful magnet[60].

Another non-invasive cancer treatment involves the use of light to induce cell death by two avenues: photothermal therapy (PTT) and photodynamic therapy (PDT). Photothermal therapy involves the application of intense light from a laser to a specific point on the body to heat up cells to induce cell death. This method is best utilized on skin or near-skin sites and is particularly useful against skin infections and cancer. The process, however, often requires contrast agents to increase heat absorption and patients are subject to sun sensitivity and adverse effects around the target area due to non-specific light absorption.

Photodynamic therapy begins by adding a photosensitizer (PS) to the target area and then applying light, typically in the form of a laser, to the location. The PS, upon absorbing an applied photon, quickly exchanges energy with its surroundings to yield reactive radical molecules or singlet-state oxygen. Both products are highly destructive to biomolecules in the immediate area, thus an application of PDT at significant scale is capable of inducing cell death[61,62,63,64.]

The same strategy to deliver drugs can be used to deliver other elements, such as photosensitizers. Intravenous distribution of PS for photodynamic therapy are hindered by similar problems as chemotherapeutic drugs, such as poor solubility, delivery, and

poor specificity. Engineered nanoparticles can contain PS molecules in a stable environment for release at the target site[60].

Photothermal therapy can be improved using nanoparticles as the contrasting agent. Small copper[65] or gold nanoparticles are common, due to the ability to adjust absorbance to optimal laser frequencies simply by changing nanoparticle size[66]. Metal nanoparticles and potential for functionalization allows for far more specific application of the contrast agent. Furthermore, the same particles used for photothermal contrast can be used as delivery vehicles for photosensitizing agents or other drugs[63,67]. We have approached this topic previously with some variation[68], one of which is described in Chapter 1.

Liquid Biopsies for Cancer Detection, Diagnosis, and Prognosis. In the field of oncology, the most common tool for tailoring treatment options to a patient is to acquire a piece of the cancerous tissue and analyze it directly. Tissue biopsy, however, is invasive, costly, rarely repeatable, and not viable for some cancer types or patient situations. Additionally, tumor heterogeneity and tendency to mutate limits the time in which a biopsy can be considered an accurate source of information. An ability to detect, measure, and diagnose cancer through simpler methods is highly desirable, and indeed possible through various methods of liquid biopsy. In addition to avoiding invasive surgeries and being more widely accessible, liquid biopsy allows for repeat testing and analysis to analyze changes in tumor behavior and treatment effectiveness. Comprehensive molecular profiling of blood samples can yield genetic information from tumors from blood and is already used in conjunction with tumor biopsies[69,70].

Liquid biopsies aim to detect or characterize four distinct types of circulating material shed from the parent tumor: nucleic acids, proteins, vesicles, and circulating tumor cells (CTCs). Circulating tumor DNA and RNA, released by tumor cells which are frequently apoptotic or necrotic, is unique to the tumors present in most cancer patients and detected by PCR-based technologies[71]. Circulating tumor proteins, shed or excreted from cancer cells or by the human body responding to cancerous symptoms, are typically measured by western blot, enzyme-linked immunosorbent assay (ELISA), radioimmune assays, or mass spectrometric methods[72,73]. Extracellular vesicles of tumor origin are of greater importance due to their ability to package wide ranges of proteins and nucleic acids within their membrane, which can deliver these payloads to other cells[74], a dangerous prospect to cells near cancerous tissue.

The paramount indicator of cancer in blood[75], circulating tumor cells are the hallmark of invasive cancer behavior and the direct cause of metastasis. CTCs are shed from a parent tumor, undergoing a process known as the epithelial-to-mesenchymal transition (EMT) to break off into the circulatory system. A small fraction of these circulating cells (<0.01%) will undergo the reverse process in a distant part of the body and become the seed of a secondary tumor after a second transition from the mesenchymal to epithelial environment (MET)[76]. CTCs have been found in blood before the parent tumor was even detectable to standard techniques[77], and their frequency is known to be a significant indicator of patient prognosis[78,79,80]. Additionally, the likeness of a CTC to its parent tumor potentially allows for the gathering of information previously only determined by direct biopsy.

There are significant barriers to the development of a cancer liquid biopsy system. Detecting RNA, DNA, vesicle, or CTC analytes requires exceptionally rigorous sensitivity and selectivity because these cancer byproducts are surrounded by similar materials yielded during normal operations of the human body. In whole blood, the fraction of DNA yielded from a cancer source was found to be frequently less than 1% of total DNA in the sample[67]. Blood is inundated with proteins of up to 40,000 different distinct uses, of which only a few may be cancerous in origin and therefore extremely difficult to isolate[68]. Circulating tumor cells are exceptionally rare; in one milliliter of blood, as few as one tumor cell may be found amongst up to one million white blood cells and 5 billion red blood cells[74]. As such, typical quantification methods such as Western Blot, enzyme-linked immunosorbent assay (ELISA), and polymerase-chain reaction (PCR) lack the sensitivity to distinguish the normal from the cancer-derived.

Of the circulating biomarkers, circulating tumor cells have been identified as the most reliable target for liquid biopsies[71]. CTCs which were nearly identical to the parent tumor were first described in 1869 by Thomas Ashworth, who immediately theorized their potential role in spreading cancer in a single patient. Tumor cells that complete the transition typically survive just a short time, between 1 and 3 hours due to rapid loss of epithelial contact and triggered apoptosis. In circulation, CTCs are between 10 and 30μm in size and exist as rigid, rough spindles, a considerable morphological change from the cubic shape more typical of a cell of epithelial origin. Only 0.1% of CTCs survive the stresses of circulation to remain viable for metastasis[72].

Metastatic behavior is dictated by one of two prevailing theories. First is the well-known seed-and-soil theory, stating that CTCs (the seeds) only anchor into and produce

secondary tumors in sites that are suited for their support (the soil). This is based on the observation that certain cancer types will tend to metastasize to specific organ types at the exclusion of others and proven in the discovery of chemokine ligand production in cancer cells. Chemokine specificity influences CTC anchoring by emphasizing which types of cells they will interact with. The second theory simply states that blood flow direction is all that determines metastatic location and CTC anchoring is decided by their size and likelihood of being lodged in a capillary (human capillaries can be as small as 8μm, one red blood cell diameter, too thin to fit rigid CTCs) during transit. This theory is supported by evidence of secondary tumor appearance despite no evidence of transformation that produces chemokines or other promoters. Evidence of both circulation theory and seed-and-soil theory appear in clinical examinations, indicating that the theories together explain the mechanism of metastasis[81].

The mechanism of metastatic evolution yields several key characteristics that can be exploited in liquid biopsy. Cells shed by a primary tumor must necessarily undergo a certain degree of change during EMT, in which the cell changes from that of an epithelial affiliation to one that can circulate. This transition results in a change in cell shape and morphology described above, as well as altering surface marker expression such as the presence of cadherin and other adherent surface proteins. ‘Successful’ transition to produce a viable cell capable of seeding a secondary tumor requires the repression of anoikis, the self-apoptotic process that tissue cells traditionally anchored to the extracellular matrix undergo when they disconnect from the environment. Occasionally, EMT will prompt the evolution of stem cell characteristics, yielding cancer stem cells (CSCs). The result of these transitions, combined with the inherent heterogeneity of the

parent tumor, is that CTCs can be very heterogeneous in character, especially in surface marker expression[77].

149 years after their discovery, detection of CTCs in human whole blood remains challenging. The last 15 years have seen extraordinary growth in detection capability, though very few methods have reached clinical approval[82]. CTC rarity cannot be overcome by bulk analysis alone: quickly the blood volume necessary to reliably detect CTCs in a system such as flow cytometry becomes prohibitively high. As such, detection platforms almost ubiquitously use an enrichment technique to concentrate CTCs from a larger volume to ease detection.

Gold nanoparticles offer an opening to generate the necessary sensitivity and specificity needed to analyze such rare events. Strong absorption and augmentation of fluorescent and Raman dyes can amplify signals produced by small populations otherwise difficult to elucidate, such as single proteins or vesicles. The increases in sensitivity of Raman and fluorescence detection above, and other manipulations of gold nanoparticle properties, give rise to experimental sensitivities several orders of magnitude lower than more standard methods. The use of gold nanoparticles for diagnosis and treatment is well-studied and reviewed, and their use in detecting circulating biomarkers has gained significant traction in recent years[83].

Gold Nanoparticles in Early Cancer Detection. As addressed above, the rarity of CTCs in the context of whole blood samples requires the use of sensitive and specific techniques to isolate, detect, and analyze these cells. Over 400 devices and techniques have been developed to do exactly this, however, only one has been accepted by the US Food and Drug Administration (FDA) for clinical use[80]. This technique, known as the

CellSearch system by Veridex, uses 120-200nm iron nanoparticles embedded with Epithelial Cell Adhesion Molecule (EpCAM) antibodies to immunomagnetically isolate circulating tumor cells from blood. CellSearch then uses a follow-up fluorescent-labeled cytokeratin antibody to count the captured cells via flow cytometry. This technique has demonstrated success in various adenocarcinomas but has a detection rate of just 50% for patients known to be afflicted by metastatic tumors. Additionally, the technique requires many hours to undergo a complicated isolation process that can adversely affect the sensitivity[84].

Of the hundreds of methods produced as alternatives, many utilize gold nanoparticles to circumvent the limitations of earlier procedures. A few directly utilize the easy modification and high surface area of gold nanostructures. For example, capturing CTCs on a functionalized gold substrate can be significantly improved by adding adhered nanoparticles or inlaid nanostructures to otherwise featureless devices that vastly increase the surface area or preferentially restrict the movement of cells of a size or shape range. The result is a massive increase in capture efficiency from 49% in solid surface designs to over 90%[85]. A unique method utilizes the gold surface of nanoparticles to detect CTCs by measuring the current produced as these particles catalyze the hydrogen evolution reaction (HER). Targeted particles, aided by immunomagnetic separation, managed to capture and detect the current produced by just 160 labeled cells[86,87]. Targeted gold nanoparticles are also detectable in blood with instruments such as high-resolution synchrotron x-ray micro-imaging[88].

Other examples focus on exploiting the optical properties of gold nanoparticles to increase detection capability. Surface-enhanced Raman spectroscopy has proven

especially useful in this field by providing considerable advantages over fluorescence, as discussed earlier. Gold nanoparticles can be developed into SERS nanoparticles by coating (chemically or electrostatically) with a Raman-active dye molecule and then stabilizing the particle, typically with a biocompatible material. The first demonstration of the use of SERS NPs for detecting CTCs was shown by Sha *et al.* in 2008, in which 50nm Au NPs were labeled with human epidermal growth factor receptor 2 (HER-2) antibodies and used to detect a mimic of CTCs, dispersed SK-BR-3 breast cancer cells enriched by immunomagnetic separation with anti-EpCAM. This first attempt demonstrated a linear relationship between cell count and Raman intensity, as well as a limit of detection of just 10 cells per milliliter of blood analyzed[89]. Further modification of this method placed the cells under a flow condition across the capture magnet, which allowed for the entire volume of blood to be subjected to far greater magnetic influence[90].

Nie and partners demonstrated the clinical potential of CTC detection using SERS nanoparticles embedded with small-molecule epidermal growth factor (EGF), the Raman-active QSY-21 molecule, and density gradient centrifugation. Typically, centrifugation is an unreliable separation technique due to the similarity of CTCs in size and density to white blood cells (WBCs) and the immune system's tendency to nonspecifically bind antibodies. This system, however, targeted the epidermal growth factor receptor (EGFR) expression of head and neck cancers with the receptor ligand. The result was a successful detection of CTCs in 17 of 19 metastatic patients and a limit of detection between 5 and 50 CTCs/mL[91].

The platform developed by our group in the last ten years integrates the capture and detection method into a single iron oxide-gold (IO-Au) core-shell nanoparticle

population. The gold surface provides easy modification, biocompatibility, and the strong plasmon resonance necessary to improve SERS detection while the magnetic core provides a separation avenue. The IO-Au NPs are modified through the addition of QSY-21 dye, PEGylation, and antibody conjugation, then mixed directly with whole blood to bind to CTCs directly. This mixture is followed by one-step magnetic separation and enrichment by flowing the entire volume of blood through a capillary tube adjacent to a magnet, and then detected on-line with SERS. This method was improved with the use of asymmetric IO-Au nanoovals (NOVs) that promote higher SERS activity over spherical particles and by targeting both EpCAM and HER-2 simultaneously. These dual-targeted NOVs successfully captured 90% of SK-BR-3 cells spiked in whole blood without interference from free NOVs. The method achieved an unprecedented limit of detection of 1-2 cells/mL[92].

Multiplexed SERS NPs allows for multicolor imaging of a single target cell, as demonstrated by Nima *et al.* using silver-coated gold nanorods to determine the presence of four separate surface markers on breast cancer cells in a solution of WBCs. Four separate populations of silver-gold nanorods were mixed with an antibody for one of the following: insulin growth factor 1 receptor (IGF-1R), EpCAM, CD44, or Keratin 18. Each population was tagged with a different Raman reporter, and all four solutions were mixed with tumor cells spiked into a WBC solution. This process allowed for the degree of expression of four proteins on of one cell to be evaluated in a single step and demonstrates the capability of the characterization of CTCs in a consolidated platform[83,93].

CHAPTER 3

Development of a Modified Antibody Conjugation Technique for Gold Nanorods and Iron Oxide-gold Core-shell Nanoparticles

Introduction

As outlined in the review, gold nanoparticles are often not synthesized and immediately ready for use. Modification of the surface is required for two purposes: to prepare the nanoparticle with the proper chemical augments and stabilizing matrix[46]. The first is dependent on the purpose of the experiment while the second is dependent on the experimental conditions. The nanoparticles must be modified to perform the task of interest while remaining stable and functional.

Future work in developing novel cancer detection methods required 'in-house' development in both avenues. The group required a SERS-active nanoparticle with and without immune targeting implements, and the same particles to be stable in physiological conditions. Prior nanoparticle conjugation procedures[87] were no longer viable for two reasons. First, the procedure for producing core-shell nanoparticles no longer interacted favorably with commercially-provided iron oxide cores, which necessitated the generation of new core-shell nanoparticle procedures, as published by Kwizera *et al.*[94]. Second, the prior antibody conjugation procedure was not optimized for retaining SERS activity throughout the experiment. Previous methods of gold nanoparticle conjugation involved coating the nanoparticle's gold surface with a mixture of 5kDa carboxylic acid-polyethylene glycol-thiol (COOH-PEG-SH) and methyl-polyethylene glycol-thiol (mPEG-SH), displacing the CTAB capping agent in favor of the biocompatible PEG. This was followed by carbodiimide crosslinking reaction to

couple a carboxylic acid and a primary amine via the creation of an amide bond[87]. This process, however, required no less than nine centrifugation steps between the addition of the Raman-active dye molecules (added prior to PEGylation) and the final purification of nanoparticles ready for experimentation. Figure 3.1 displays the SERS activity of 750nm gold nanorods labeled with 20,000:1 QSY-21 Raman-active dye subject to multiple centrifugation steps after PEGylation. By the third centrifugation step, we see a SERS activity at just 20% of the original signal strength and the ninth centrifugation step eliminated more than 95% of the SERS activity. This revealed a need to explore methods that required fewer purification steps between the application of dye and completion of the preparatory steps.

Here the development of an alternate method for antibody conjugation to gold-surfaced nanoparticles is reported. Utilizing a pre-modified linking PEG and convergent synthetic strategy, SERS-active nanocomplex assembly is produced and proven through the demonstration of selective binding with five antibodies and four cell lines.

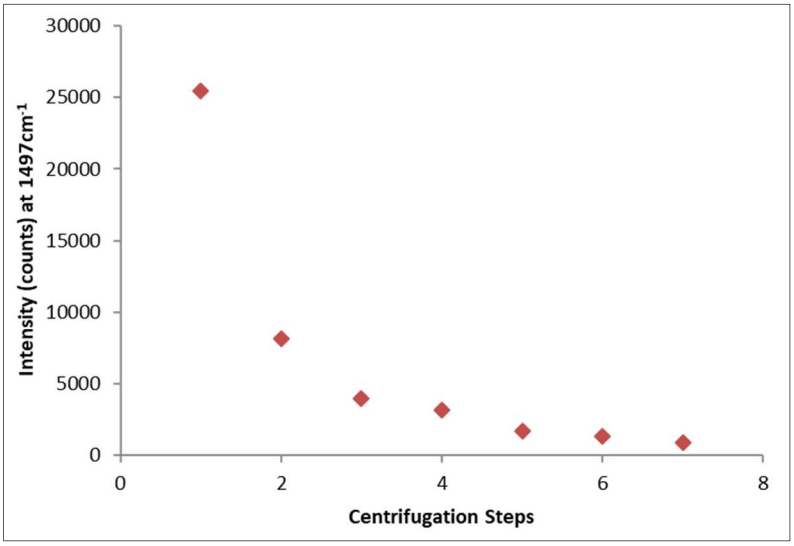

Figure 3.1: The effect of multiple centrifugation steps on SERS activity of QSY-21 dye-labeled gold nanoparticles.

Experimental Methods

Horseradish Peroxidase PEG Modification. Modification of Horseradish Peroxidase (HRP) with N-hydroxysuccinimide-polyethylene glycol-thiol (NHS-PEG-SH (5k MW)) was carried out through a modified carbodiimide linking procedure under buffered conditions. Briefly, powdered horseradish peroxidase dissolved in one of the following buffers: phosphate-buffered saline (PBS) (pH 7.3), 0.01M bicarbonate buffer (pH 8.4), and 2-(N-morpholino)ethanesulfonic acid (MES) buffer (pH 5.5). The desired concentration was 0.33mg/mL protein solution. 10μL of this solution was rapidly vortexed with varying volumes of 0.1μM to 10mM NHS-PEG-SH dissolved in a matching buffer. The solution was then immediately placed in an ice bath and kept at 4°C for 16 hours. In one exception listed below, the solution was kept at room temperature (~23°C) for comparative study. The solution was then purified by centrifuge filtration (10,000 MW pass filter) with three washing steps. Remaining product was redispersed in water. Modification strength of each synthesis was measured by mixing 100μL of 1:1000 diluted HRP-PEG-SH with 25μL of 1-Step Ultra TMB-ELISA Substrate Solution (ThermoFisher Scientific, hereafter 'TMB assay') for five minutes and the color change was observed. Verification of the modification of HRP was conducted by adding a droplet of the purified solution to a gold-coated glass slide, adjacent to a droplet of unmodified HRP solution. After twenty minutes, the droplet was washed away and 1μL of TMB assay was added to the location of both spots. After five minutes, the solution was removed and placed on a clear glass slide for visualization of the color change.

Antibody PEG modification. Modification of antibodies with NHS-PEG-SH was completed in a slightly modified procedure based on results from the HRP

modification detailed above. 10µg of stock antibody in solution was washed once with centrifuge filtration to remove sodium azide preservative. Buffer exchange was carried out when testing antibody modification with BC buffer. The solution was then rapidly mixed with 10µL of 1mM NHS-PEG-SH by strong vortexing. The solution was then placed in an ice bath and kept at 4ºC for 16 hours, before purifying four times with centrifuge filtration (10,000 MW pass filter). Product was dispersed in water.

Thiol-PEG Modified Horseradish Peroxidase Conjugation to Gold Nanoparticles

Gold nanorods and iron oxide-gold core-shell nanopopcorn (NPCs) were conjugated with HRP-PEG-SH using the following method with a range of parameters investigated. First, reaction stir time was investigated. Modified HRP was added to a 250µL solution of 1nM gold nanorods and stirred at 260 rpm for up to 16 hours, with samples stopped at 2, 4, 6, 8, and 16 hours. Afterward, the gold nanorods were mixed with 50,000:1 methyl-polyethylene glycol-thiol (mPEG-SH 5k MW) for thirty minutes and then purified by centrifugation (10,000rpm, 10 minutes). Centrifugation was repeated four times with the supernatant collected at each step. 100µL of each supernatant and the purified gold nanorod solution was mixed with 25µL of TMB assay and observed for twenty minutes to view color change.

Next, the temperature and reaction buffer of the HRP modification step was analyzed in terms of how it affected nanoparticle conjugation. Four units of HRP were modified, two each prepared in PBS and BC buffer, and one of each buffered set was incubated at room temperature (between 22-23ºC) for 16 hours. After purification and redispersal in ultrapure water as described above, the modified HRP solutions were each

mixed with separate aliquots of 250µL solution of 1nM gold nanorods and stirred for 8 hours, followed by mPEG modification for thirty minutes. Purification was carried out via four centrifugation steps in which the supernatant was collected. 100µL of each supernatant and the purified gold nanorod solution was mixed with 25µL of TMB assay and observed for twenty minutes to view color change.

Finally, modified HRP was conjugated to gold nanoparticles for the purpose of determining optimum time to add Raman-active dye molecules to the nanorods for the production of SERS-active conjugates. Six aliquots of PBS-prepared HRP-PEG-SH were mixed with six gold nanorod solutions and stirred for 8 hours, followed by mPEG modification for thirty minutes. QSY-21 Raman-active dye was added (at 20:000 dye molecules per gold nanorod) at six varying steps, with each solution used to test one addition time. These times were at the start of conjugation, at 4, 6, 7, 7.5, and 8 hours. Purification was carried out via four centrifugation steps in which the supernatant was collected. 100µL of each supernatant and the purified gold nanorod solution was mixed with 25µL of TMB assay and observed for twenty minutes to view color change. 10µL aliquots of the gold nanorod solutions were collected after the first purification step and diluted to 100µL. 5µL droplets of these solutions were interrogated with a Raman Spectrometer (TSI, Inc. EZRaman Reader, λ=785nm laser) at 1s integration time and 25mW laser power. The intensity at 1497cm^{-1}, corresponding to the strongest reporting peak of the QSY-21 Raman spectrum, was recorded.

Thiol-PEG Modified Antibody Conjugation to Gold Nanoparticles. Antibody conjugation of gold nanoparticles was then attempted using the most optimal conditions established in previous experiments. 10µg of antibody (anti-Human Epidermal Growth

Factor Receptor-2 (HER2), anti-epithelial cell adhesion molecule (EpCAM), epithelial growth factor receptor, anti-CD44, and anti-insulin-like growth factor-1 receptor (IGF-1R) was modified using the reaction detailed previously and subsequently mixed with 250μL of 1nM gold nanorods or 0,025nM NPCs and stirred for 7.5h. 20,000:1 QSY-21 dye was then mixed with the nanoparticle solution for five minutes, followed by thirty minute stirring with 50,000:1 (nanorods) or 1,000,000:1 (NPCs) mPEG-SH. Particle solutions were purified twice by centrifugation.

Cell Culture and Cell Labeling Experimentation. Human breast cancer cells SK-BR-3, MCF-7, MDA-MB-468, and MDA-MB-231 were cultured in appropriate media (RPMI 1640 with 10% fetal bovine serum for SK-BR-3 and DMEM with 10% fetal bovine serum for MCF-7, MDA-MB-468, and MDA-MB-231) under 5% CO2 at 37ºC. To label cells with antibody-conjugated gold nanorods or NPCs, eight-well chambered glass slides were seeded with cells of the desired line at 50% confluence and cultured in the appropriate medium overnight. The next day, the medium was removed and replaced by a solution made from 10μL of 1nM antibody-conjugated gold nanoparticles added to 200μL of cell culture medium and allowed to incubate at 37ºC for two hours. The medium was removed, the wells washed with PBS, and the cells were fixed with 4% paraformaldehyde. Cellular binding was observed via dark field microscopy with an Olympus IX71 inverted microscope.

Results and Discussion

Previously, successful conjugation of antibodies to gold nanoparticles was observed through the lengthy process of mixing with marker-positive cells and viewing them under dark field microscopy. For the purposes of developing a new conjugation

method, this was prohibitively expensive and time-consuming for a low throughput of method variations. Additionally, prior work indicated that direct protein measurement by Coomassie Blue staining was inhibited by side reactions with CTAB and the presence of nanoparticles. In this study, the protein horseradish peroxidase (HRP) was used as a model for antibodies in nanoparticle conjugation. Substituting HRP as the protein conjugate allowed direct measurement of protein concentration via HRP oxidation of 3,3',5,5'-Tetramethylbenzidine (TMB) with H_2O_2. TMB serves as a hydrogen donor for peroxidase proteins and produces a vibrant color change dependent on the initial concentration of HRP. This process is shown in Figure 3.2. Progressive TMB oxidation was viewed as the formation of a blue color (one-electron oxidation state), which was followed by green and eventually yellow as the diimine product forms. This progressive reaction is used commonly in enzyme-linked immunosorbent assay (ELISA) and immunochemical staining, allowing for qualitative and quantitative applications[95].

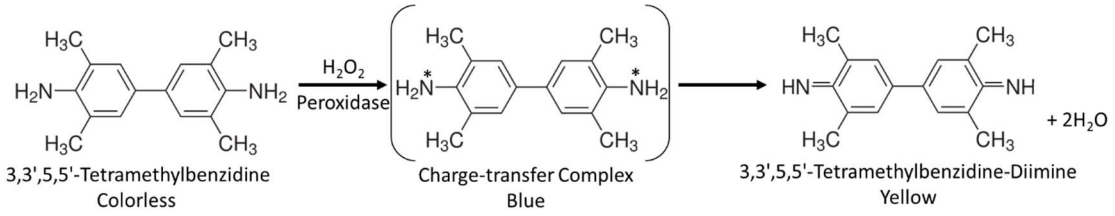

Figure 3.2: Schematic of TMB interaction with peroxidase protein in the presence of hydrogen peroxide. In the charge-transfer complex, a positive charge can be carried on either or both nitrogen atoms and the molecule forms a complex with other TMB molecules.

Horseradish peroxidase conjugation to gold nanoparticles is designed in a similar fashion to antibody conjugation, with a few differences of note. While HRP must retain its structure to function properly, like antibodies, it is not limited in orientation as the active site is not blocked by the nanoparticle presence. Additionally, at 40kDa HRP is

much smaller compared to antibodies which allows for a higher packing of protein on the nanoparticle surface. For these reasons, HRP conjugation success was used as a guiding tool to demonstrate good alternate conjugation practice and evaluated qualitatively. It is acknowledged that quantitative techniques can be applied in a more focused and rigorous study of HRP-nanoparticle conjugation.

Horseradish Peroxidase and Antibody PEG Modification. The chosen linking polymer for nanoparticle conjugation was N-hydroxysuccinimide-polyethylene glycol-thiol (NHS-PEG-SH). The rationale for this decision lays in prior work with carbodiimide linking, in which the latter required ethyl(dimethylaminopropyl)carbodiimide (EDC) activation of carboxyl groups on carboxy-PEG-SH polymer coating gold nanoparticles. The repeat centrifugation steps to purify both the PEG-nanoparticles and then the conjugated nanoparticle product could be eliminated if the carbodiimide linking reaction was carried out before the linking PEG molecule was attached to the nanoparticle. NHS-PEG effectively accomplishes this by providing an activated carboxyl group for carbodiimide linking pre-modified on the PEG-SH scaffold. This functional group rapidly hydrolyzes under room temperature and at high pH, thereby requiring the reaction to be carried out at low temperature and in a buffered solution.

Antibody and HRP modification with NHS-PEG-SH was carried out in phosphate-buffered saline (PBS) (pH 7.4), 0.01M bicarbonate buffer (pH 8.1), and 2-(N-morpholino)ethanesulfonic acid (MES) buffer (pH 5.5). NHS-PEG-SH was mixed with HRP at a range of ratios from 100:1 to 1,000:1. Using 10µL of 0.33mg/mL HRP, the additions of NHS-PEG-SH ranged from 8.25µL of 10µM solution to 10µL of 10mM. The

NHS-PEG-SH was dissolved in cold buffer and immediately dispensed into the HRP solutions and left still for 16 hours at 4°C or at room temperature. The modified HRP was isolated by 10k MW centrifuge filtration and washed three times with ultrapure water. TMB assay application to 1:1000 dilutions of these solutions produced the strongest response at 100:1 ratio, indicating a maximum of NHS-PEG-SH linking without degrading or disrupting the HRP's functionality. Reactions in MES buffer produced poor or no response to TMB assay and were thus discarded, but PBS and BC buffer showed minimal difference in effectiveness. HRP-PEG incubated at 4°C produced a reliable TMB turnover relative to room temperature incubation. Verification of HRP-PEG-SH attachment was carried out by adding a drop of solution to the surface of a gold-coated glass slide for twenty minutes, during which the thiol end of the linking PEG would adhere to the gold surface of the slide. After removal of the solution and repeated washing, TMB reagent was added to the coated spot and the color change was observed for five minutes. Rapidly the solution turned yellow, indicating a successful binding of HRP to the gold surface, and therefore the PEG-SH linker's presence on the protein.

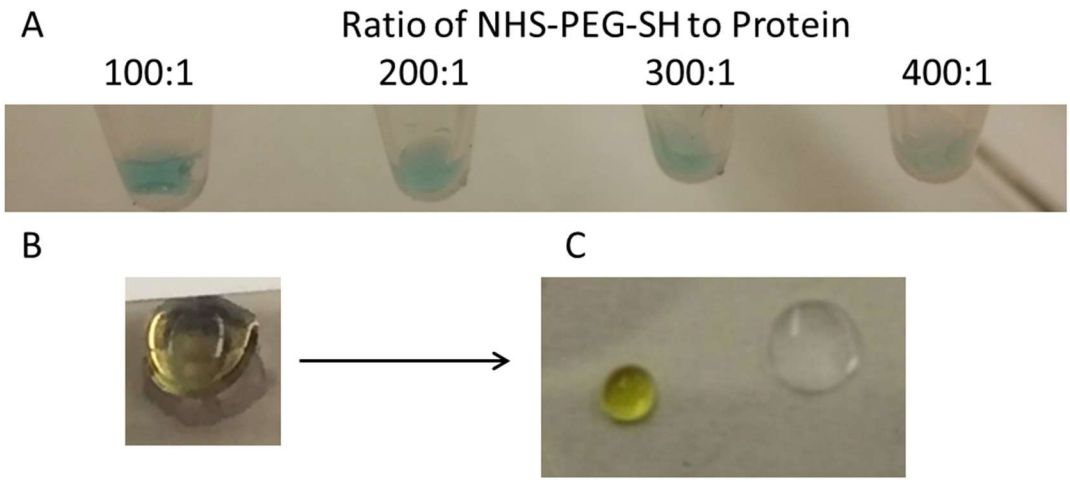

Figure 3.3: A) Twenty-minute TMB assay product of NHS-PEG-SH and Horseradish peroxidase mixed at different ratios overnight. B) Five-minute TMB assay of HRP-PEG-SH adhered to gold-coated glass slide. C) Left: Liquid component of the TMB assay of HRP-PEG-SH on gold-coated glass slide shown in B, as visualized on glass coverslip Right: Liquid component of TMB assay of unmodified HRP placed on gold-coated glass slide for comparison.

Thiol-PEG Modified Horseradish Peroxidase Conjugation to Gold Nanoparticles

Next, nanoparticle conjugation was explored with modified HS-PEG-HRP. 3.3µg of HRP-PEG-SH was prepared as described (100:1 PEG: protein ratio) and mixed with 250µL of 1nM gold nanorods (a 400:1 ratio of protein to nanoparticle) at slow speed for time periods between 1h and 16h. Nanorods were then mixed with 5kDa methyl-polyethylene glycol-thiol (mPEG-SH) at 50,000:1 for thirty minutes before purification by centrifugation. Five purification steps were carried out, with the supernatant collected at each step. Each supernatant, along with an equal volume of modified nanorods, were tested with TMB assay to determine the presence of HRP independent of the supernatant. It was found that the optimum reaction time was between 6 and 8 hours, with 8 hours producing the strongest response. All gold nanorod solutions

produced stronger color changes relative to the third and fourth supernatant collected, verifying that the HRP was attached to the nanorods.

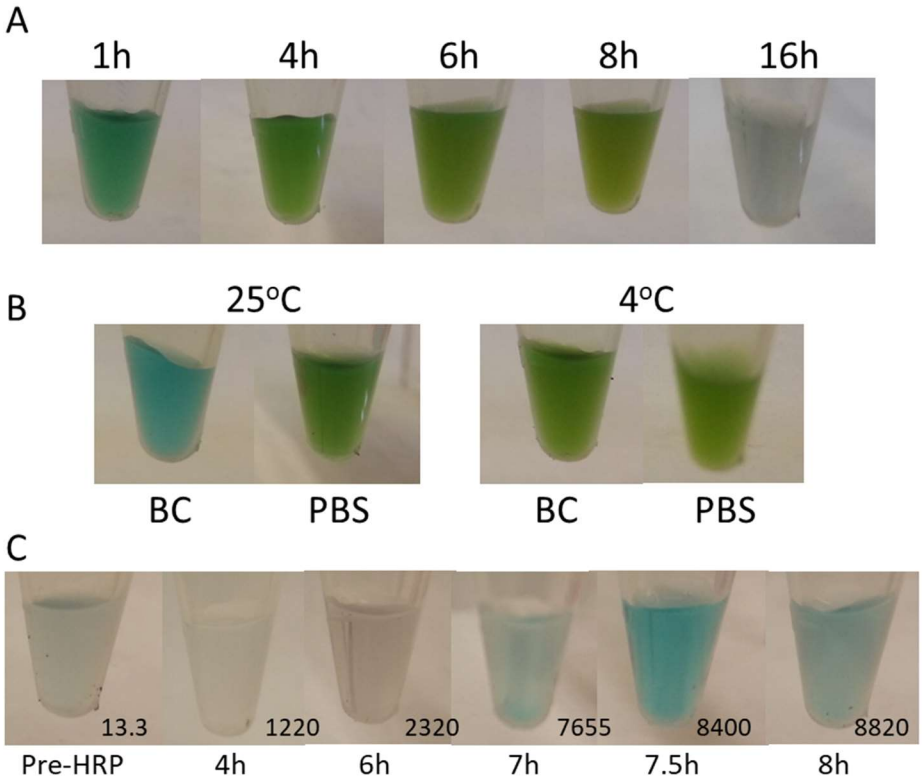

Figure 3.4: TMB assay results of gold nanorod conjugation with thiol-PEG-modified HRP. A) TMB assay of purified gold nanorod solutions mixed with HRP-PEG-SH between 1 and 16 hours. B) TMB assay of purified gold nanorod solutions mixed with HRP-PEG-SH prepared at room temperature or at 4°C in bicarbonate buffer or phosphate-buffered saline. C) TMB assay of 1:100 diluted purified gold nanorod solutions mixed with HRP-PEG-SH and labeled with QSY-21 dye at the listed times. Raman response (in counts at 1497cm^{-1}) for each nanorod solution is inset.

With an optimum reaction time and ratio established, the addition of a Raman-active dye was incorporated into the process. Several aliquots of nanorods were tested by adding 25,000:1 QSY-21Raman reporter at various times during the stirring process: prior to HRP-PEG-SH addition, and then at two-hour intervals after HRP-PEG-SH mixing, with an additional test at 7.5h. Each solution was then mixed with mPEG-SH and purified as described previously. 10µL aliquots were removed from the solutions after the

first centrifugation diluted to 100µL with ultrapure water for Raman analysis. As before, four purification steps were completed, and the supernatant preserved. TMB assay analysis of both dye-adsorbed HRP-PEG-NRs and supernatants was conducted, with a clear indication that the addition at 7.5h preserved HRP adherence to gold nanorods while producing strong Raman spectra.

Thiol-PEG Modified Antibody Conjugation to Gold Nanoparticles. The optimized HRP conjugation procedure was used as a starting point to conjugate antibodies to gold nanorods. Due to differences in antibody charge distribution, both PBS and BC incubation buffers were tested. 10µL of 1mg/mL of anti-Human Epidermal Growth Factor Receptor-2 (HER2) antibody was mixed at 1:100 ratio with NHS-PEG-SH and incubated at 4ºC for 16 hours, and then purified by 10kDa centrifuge filtration. The Ab-PEG was re-dispersed in ultrapure water and mixed with 250µL of 1nM gold nanorods (400:1 ratio) for 7.5 hours, mixed with 20,000:1 QSY-21 Raman reporter for five minutes, then mixed with 5k mPEG-SH for thirty minutes. The resulting solution was purified by one centrifugation step, and redispersed in PBS.

Cell Labeling Experimentation. Verification of antibody conjugation was carried out by adding 10µL of 1nM anti-HER2-PEG-NPCs to 200µL of cell culture medium distributed into eight-chambered cell culture slides with breast cancer cell lines. SK-BR-3 was chosen as the HER2-positive control while MDA-MB-468 was chosen as the HER2-negative control. After incubating for two hours at 37ºC, the medium was extracted, cells were washed and fixed, and the slides analyzed under dark field microscopy. Positive antibody conjugation was indicated by the prominent coating of gold nanoparticles on cells which expressed the marker. It was found that PBS-incubated

anti-HER2-PEG-nanorods rapidly and thoroughly coated SK-BR-3 cells while not interacting with MDA-MB-468 cells and was vastly superior to BC-incubated anti-HER2-PEG.

This success was used to transfer the procedure to iron oxide-gold core-shell nanopopcorn (NPCs) chosen for their combined magnetic and SERS capability. Due to the increased size of NPCs relative to the gold nanorods, varying ratios of anti-HER-2-PEG-SH were mixed with 250µL of 0.025nM NPCs from 1000:1 to 24,000:1. Dark field microscopy of SK-BR-3, as shown in Figure 3.5, revealed a successful conjugation at all four ratios tested with an increase in cell labeling relative to the increased antibody-PEG up to 16,000:1. 24,000:1 revealed no significant difference in cell labeling.

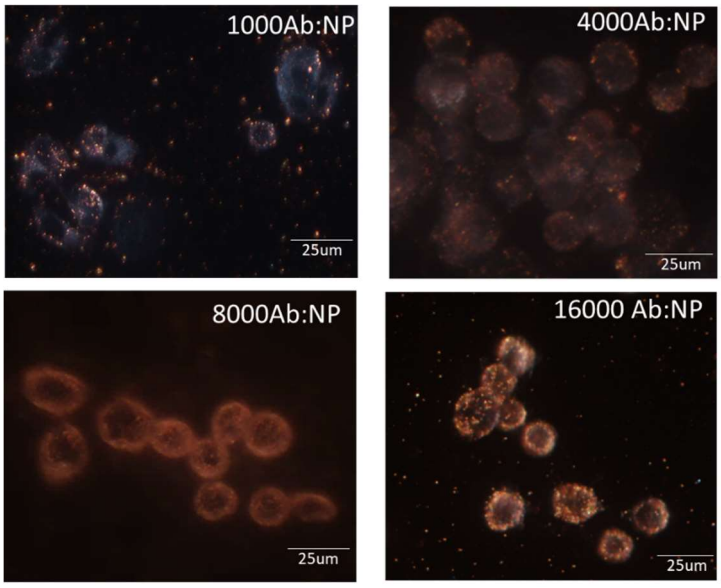

Figure 3.5: Dark Field Microscopy of cells incubated with anti-HER-2-PEG-NPCs for two hours. The ratios of antibody per particle in the conjugation mixture are given.

The successful conjugation of anti-HER-2 to NPCs demonstrated the merit of the procedure and it was therefore extended to other antibodies, including anti-epithelial cell adhesion molecule (EpCAM), epithelial growth factor receptor, anti-CD44, and anti-

insulin-like growth factor-1 receptor (IGF-1R). Breast cancer cell lines were chosen as the positive and negative controls for each: SK-BR-3 EpCAM positive, EGFR/IGF-1R/CD44 negative; MDA-MB-468 EpCAM/EGFR positive, IGF-1R/CD44 negative; MCF-7 EpCAM/IGF-1R positive, EGFR negative; MDA-MB-231 CD44 positive, EpCAM/EGFR/IGF-1R negative. Notably, only anti-EpCAM and anti-CD44 were found to be more effective when modified with the NHS-PEG-SH in BC buffer, while anti-EGFR and anti-IGF-1R were more effectively modified when incubated in PBS. The detailed result of these experiments can be found in Figure 3.6. Overall, the results of this experiment strongly align with known cell line expressions, as confirmed with flow cytometry.

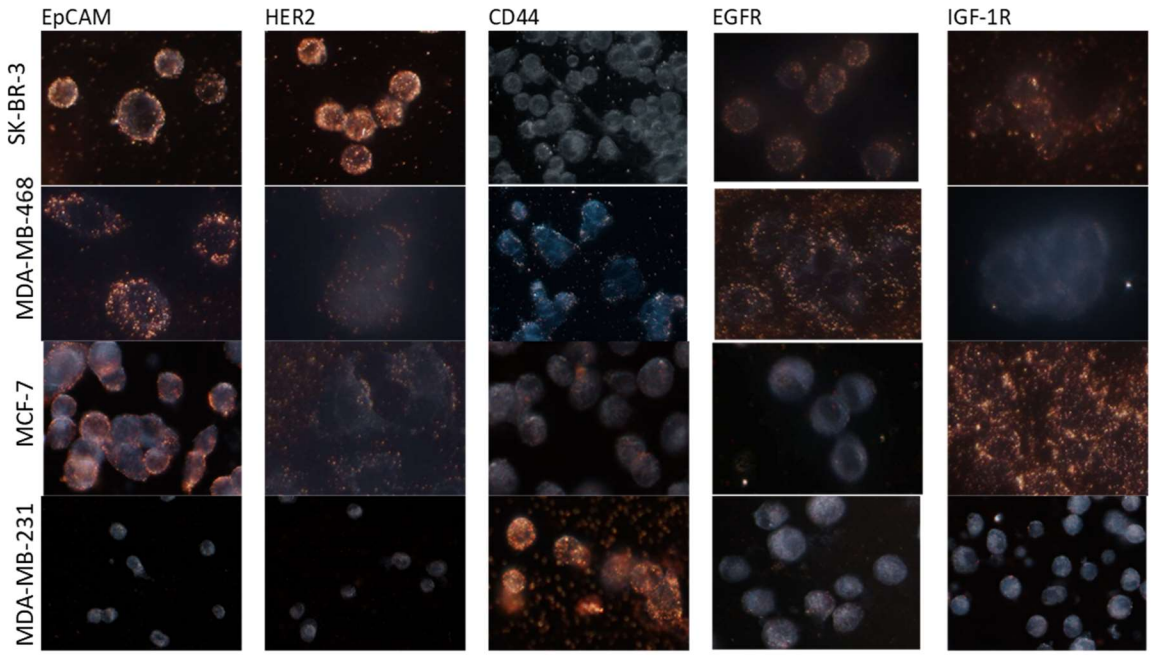

Figure 3.6: Dark field microscopy of four breast cancer cell lines after two-hour incubation with antibody-PEG-NPCs targeting the listed surface markers. All images are taken at 40x magnification.

Conclusion

A wide range of methods of antibody conjugation were attempted to preserve SERS activity and cooperate with the novel core-shell nanopopcorn developed by fellow group members. The potential of utilizing a pre-activated PEG-thiol linking molecule for this purpose was undertaken. Using horseradish peroxidase as a model for an antibody, we successfully developed a linking process that cooperates with multiple nanoparticle species. Additionally, the method requires only one or two purification steps following the addition of Raman-active dye molecules, a considerable improvement over the nine steps required by the previous method. This process transferred to antibody conjugation almost seamlessly and was proven through the successful demonstration of cell labeling with five different antibodies.

Several factors are open for more thorough exploration, such as the effect of dye addition on antibody viability and a concentrated study on the effect of pH on the interaction between NHS-PEG-SH and different antibodies. While this study did not yield direct benefits towards the concurrent photothermal/photodynamic therapy study detailed in the following chapter, it has provided an avenue for simple modification of the gold nanorods used such that a future project may involve immunotargeted nanocomplexes that further enhance the selective effect of the treatments. More importantly, this study laid the ground work for synthesizing SERS-active iron oxide-gold core-shell anti-PEG-NPC, around which the nanoparticle-based capture and detection system described in Chapter 5 is made possible.

Chapter 4

Photosensitizer-loaded Gold Nanorods for Near-infrared Photodynamic and Photothermal Therapy

Introduction

As introduced and elucidated earlier, photothermal (PTT) and photodynamic therapy (PDT) are techniques which utilize laser light to induce cell death. When used for treatment purposes, the procedures for each are localized, non-invasive, portable, inexpensive, and simple to operate. Both treatments have seen extensive use, most recently in the treatment of several cancer types from skin cancer to esophageal and lung cancer[60,61,62,63,64,65,66,67]. The limitations of both methods hinder these efforts, most especially the poor specificity of the contrast agents and photosensitizers. Considerable effort has gone in to developing nanoscale carriers for several chemical treatments in order to improve delivery and specificity.

An evolution of this development was the utilization of photothermal nanoparticles as the carrier for photosensitizer (PS) agents. This allows for a double treatment of PTT and PDT through a single application of material, potentially increasing the effectiveness of both through synergistic effects. For human treatment, the laser wavelength is tuned to the near-infrared (NIR) region to exploit a minimum in biological absorption due to water and hemoglobin in tissues. For this reason, gold nanorods have attracted significant attention due to their numerous advantages in material safety and functionality as well as simple and precisely tunable synthesis. Nanorods have previously been used for chemical delivery and phototherapy, demonstrating their usefulness[96,97,98,99,100].

Still, formulation of a dual PTT-PDT nanocomplex with highly-efficient photosensitizer delivery has remained elusive. Prior PTT-PDT strategies required the use of two laser irradiations at different wavelengths due to absorption disagreement between the two targets. For example, Kuo *et al.* have demonstrated this dual treatment using indocyanine green adsorbed to Au NRs, as well as chitosan incorporated with indocyanine green and Au NRs. However, indocyanine green has a low solubility, a low singlet oxygen yield (<0.15) and is exposed on the surface of the complex, rendering it vulnerable to biological effects in-vivo. Using a chitosan scaffold to carry this complex increases their compatibility at the cost of markedly decreasing the delivery efficiency[98].

To address these challenges, our strategy opts to construct a nanocomplex that will use a single laser frequency for both treatments, with the hypothesis that this will enable truly simultaneous PDT and PTT and a resulting increase in efficiency. To do so, we chose a PS molecule and synthesized gold nanorods (Au NRs) with similar absorption frequencies within the NIR region. The chosen molecule, silicon 2,3-napthalocyanine dihydroxide (SiNC) possesses a lambda-max at 780nm, while the gold nanorods were synthesized to a specified peak absorption at 795nm. Nonspecific absorption of the SiNC molecules to the Au NRs was stabilized with alkyl-thiol PEG (AT-PEG) linker that entraps SiNC within the hydrophobic alkyl layer on the surface of the Au NRs, leaving only the stable, biocompatible PEG exposed. The effectiveness of this dual-function nanocomplex was demonstrated through in-vitro studies to eliminate cancer cells under low-intensity NIR light.

Experimental Methods

Synthesis and Characterization of Gold Nanorods. Au NRs were synthesized using the seed-mediated growth method following procedures developed by Murphy and El-Sayed. Briefly, small Au NPs between 2 and 5nm were synthesized by reducing chloroauric acid (HAuCl4, 0.25M) in solution with hexadecetyltrimethylammonium bromide (CTAB, 0.1M) with 4o sodium borohydride (NaBH4, 0.5mM final concentration) and left to sit for three hours. The solution turned a light yellow-brown color quickly. Next, a 100mL growth solution containing 0.1M CTAB, 0.5mM HAuCl4, and 90uM of silver nitrate (AgNO3) was prepared in a 23oC water bath with moderate stirring. The solution was injected with 700uL of 80mM ascorbic acid, which reduced the gold solution slightly, turning the solution from a golden yellow to clear. 80uL of the seed solution was then injected into the solution and left still to form Au NRs over two hours. The Au NRs were purified by two centrifugation steps and resuspended in water for further use. Absorption spectroscopy and TEM confirmed the optical and morphological properties of the Au NRs, while hydrodynamic size and zeta potential were measured with dynamic light scattering.

Synthesis and Characterization of AT-PEG The AT-PEG was synthesized by linking a thiol-alkyl-carboxylic acid compound with an amine-PEG in an organic phase. Three lengths of alkyl chains were used: mercaptohexanoic acid (MHA), mercaptoundecanoic acid (MUA), and mercaptohexadecanoic acid (MHDA). To synthesize the AT-PEG of each of these, the AT component was dissolved in 4mL of DCM or DMF to a concentration of 1mM, and 1mg of NH2-PEG (5kDa) was added. To this mixture, 0.1mg of 4-(dimethylamino) pyridine (DMAP) and 0.8mg N,N'-

dicyclohexylcarbodiimide (DCC) were added and stirred overnight to form an amide bond between carboxyl moiety of the AT and the amine of the PEG. The solvent was evaporated under nitrogen and the powder reconstituted in ultra-pure water. Dithiothreitol (DTT) was added to cleave any disulfide bonds that may have formed between the polymers during the first step. Finally, the unreacted AT was separated by 3000MW centrifugal filtration. All three AT-PEG solutions were dried and reconstitution in deuterated chloroform, then analyzed with nuclear magnetic resonance spectroscopy. Additionally, NH2-PEG, MHA, MUA, and MHDA were analyzed to compare with the compounds and confirm successful coupling.

SiNC-Loading and NR Stabilization. SiNC was dissolved in dimethyl sulfoxide (DMSO) and mixed with the Au NR solution at a ratio of 50,000:1 SiNC molecules per Au NR. SiNC coordinated to the surface through electrostatic interactions over the course of gentle vortexing for 15 minutes. Then, the AT-PEG was mixed in at a ratio of 50,000:1 AT-PEG molecules per Au NR and mixed for 40 minutes. AT-PEG/SiNC/Au NRs were purified by centrifugation and reconstituted in ultrapure water. The supernatant was collected and SiNC that was not adsorbed was transferred to dichloromethane (DCM) by liquid-liquid extraction. Raman spectroscopy of the nanocomplex confirmed adsorption of the SiNC molecules to the surface and measured the concentration of un-adsorbed SiNC left in the supernatant. Finally, the nanocomplexes were analyzed using DLS to determine the hydrodynamic size and zeta potential.

AT-PEG/SiNC/Au NRs Stability and SiNC Release. AT-PEG/SiNC/Au NRs were dispersed in 1mL of three common cell culture solutions to evaluate SiNC release over time (0.5nM final concentration of nanocomplex). These were: 1x PBS (pH 7.4,

137mM NaCl, 2.7mM KCl, 4.3mM Na2HPO4 and 1.47mM KH2PO4), RPMI 1640 cell culture medium (with 10% fetal bovine serum (FBS) and 1% penicillin/streptomycin solution), and 100% FBS. The solutions were shaken while 200uL of the solution was withdrawn at specified times between 30 minutes and 360 minutes. These were centrifuged and the supernatant was mixed with DCM to extract free SiNC. The DCM was evaporated and SiNC reconstituted in DMSO to quantify release by Raman spectroscopy.

Similarly, SiNC release was measured while AT-PEG/SiNC/Au NRs were in culture medium in the presence of cancer cells. KB-3-1 head and neck cancer and SK-BR-3 breast adenocarcinoma were cultured in RPMI 1640 (with 10% fetal bovine serum (FBS) and 1% penicillin/streptomycin solution) at 37oC and 5% CO2. The cells were seeded into 96-well plates at a density of 8,000 cells per well. Medium augmented with 0.1nM AT-PEG/SiNC/Au NRs was added and the cells left to culture. At set times between 30 minutes and 360 minutes, the medium from wells was collected (each time point was repeated in triplicate). SiNC was extracted with equal volume DCM, evaporated, and reconstituted in DMSO for quantification by Raman spectroscopy. This SiNC release is expressed as a percentage of the total amount of SiNC delivered by the AT-PEG/SiNC/Au NRs that was delivered to cells.

Laser Irradiation and Cell Viability Measurement. KB-3-1 and SK-BR-3 cells were seeded into a 96-well plate at a density of 8,000 cells per well. The next day, the cells were washed with PBS and 100uL of medium containing one of the following additions: 1) AT-PEG/Au NRs, 2) SiNC, in DMSO/H2O mixture, 3) AT-PEG/SiNC/Au NRs. These three groups represent three treatment types: 1) PTT only, 2) PDT only, and

3) dual PDT/PTT. Unmodified medium was used for the control populations. NRs in groups 1 and 3 were added to produce 0.1nM, 0.3nM, and 0.5nM final concentrations to examine dosage effects on treatment efficacy. The concentration of group 2 was also varied to range between 2 and 12uM in order to match the amount of SiNC adsorbed onto the corresponding AT-PEG/SiNC/Au NR concentration. These solutions were left to incubate for two hours before being exposed to laser irradiation by an 808nm, 0.55W/cm2 laser for eight minutes (control cells were not irradiated). After the laser application, cells were washed with PBS and incubated in fresh medium overnight before cell viability was determined using the XTT toxicology assay. Cell viability was expressed as a percentage of live cells compared to the total number of live cells in the untreated control. Each application of each group was repeated in triplicate and results are expressed as an average with standard deviation.

Statistical Analysis. Cell viability assay results for each group were compared using the analysis of variance (ANOVA) technique (p=value <0.05). Post-hoc Scheffe method was applied to determine the minimum significant difference (MSD) between treatment types and concentrations used. A difference between any two applications was considered significant if the absolute value of the difference in means exceeded the MSD derived.

Results and Discussion

Synthesis and Characterization of Gold Nanorods. As per the well-discussed seed-mediated growth method, gold nanorods were grown by the anisotropic selective deposition of reduced gold on a 2-5nm precursor ‘seed’ gold sphere. CTAB behaved as the capping material while ascorbic acid was the reducing agent. Adjustments of the

AgNO3 additive controlled the aspect ratio of the synthesized rods. The purified Au NRs exist as a colloid, being capped by positively-charged CTAB arranged in a bilayer on the surface. To maximize absorption of light from the 808nm laser, Au NRs were made to an aspect ratio of 4.1-4.2, corresponding to 90µL of $AgNO_3$ in the growth solution. TEM revealed these nanorods to be, on average, 50nm in length and 12nm in width. The absorption spectrum of these nanorods showed a longitudinal LSPR peak absorption at 800nm. To examine the photothermal properties, the particle solution was irradiated with the 808nm laser at different particle concentrations and the temperature rise was monitored. It was found that at 0.1nM, the temperature rose from 23°C to 43°C within ten minutes. Au NRs at 0.5nM, subjected to the same treatment, raised the temperature to 82°C in the same period, indicating exceptional photothermal capability. Previous studies with our group show the photothermal conversion as approximately 75%. These properties are displayed in Figure 4.1.

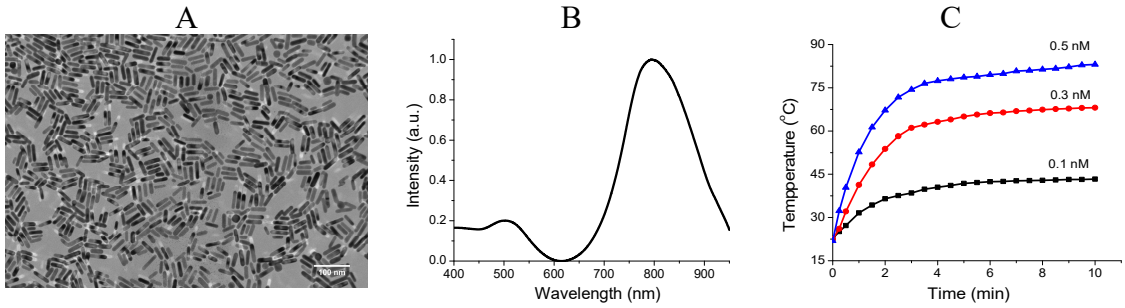

Figure 4.1: A) Transmission Electron Microscope image, B) Absorption spectroscopy, and C) photothermal properties of gold nanorods.

The CTAB bilayer is not tenable as a capping agent for Au NRs in biological applications and is easily dissociated to cause particle aggregation. To stabilize the nanoparticles for in vitro use, it is necessary to replace the CTAB with a compatible stabilizing agent. Additionally, it is necessary to stabilize the loaded SiNC molecules

after loading, and to control their preference for release from the nanocomplex in aqueous solutions. Previous work by Saheel Bhana demonstrated the capability of MUA-PEG to stabilize the hydrophobic chemotherapeutic paclitaxel to Au NRs[57]. Thus, a similar strategy was applied here, with the addition of MHA-PEG and MHDA-PEG to test the effect of AT chain length on loading and release efficiencies.

Synthesis and Characterization of AT-PEG. MHA-, MUA-, and MHDA- PEGs were all synthesized according to the DCC-activated coupling reaction. Successful amide bonding between the NH2-PEG and MHA, MUA, and MHDA was observed in the 1H NMR spectra of each species. The most notable characteristics of successful synthesis are observed by three distinct changes in 1H NMR spectra. First, there is a disappearance of a broad -COOH peak above 10ppm from the AT spectra as the carboxylic acid is aminated. Second, there is a loss of a weak peak at 1.80 attributed to the amine terminus of NH2-PEG. Finally, we observe the appearance of a new, sharp peak between 4 and 6ppm that can be assigned to the secondary amine of the newly-formed AT-PEG compound. These results confirm the successful linkage of each AT compound to NH2=PEG.

SiNC Loading and NR Stabilization. SiNC was chosen as the photosensitizer for two desirable traits. First, SiNC has a high singlet oxygen quantum yield (≥ 0.3) that ensures a reasonable conversion efficiency of incoming photons. More importantly, SiNC has an absorption spectrum that more heavily overlaps with the NIR region compared to more common clinical photosensitizers such as phthalocyanine-based molecules. As such, SiNC made an ideal choice of PS for loading onto the Au NRs.

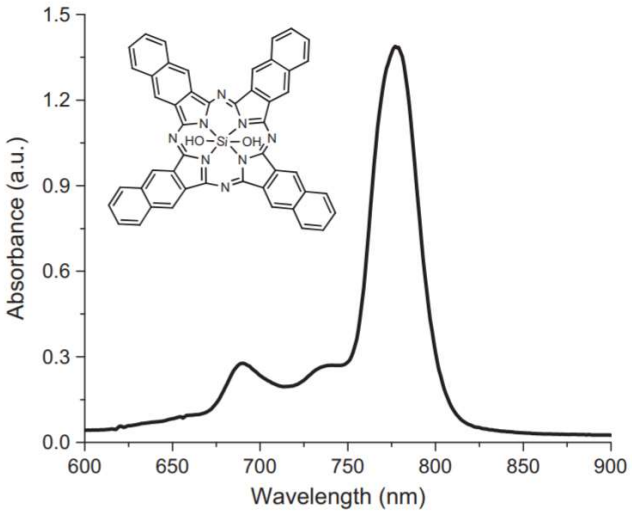

Figure 4.2: Structure and absorption spectrum of SiNC.

AT-PEG/SiNC/Au NRs were synthesized following Saheel Bhana's previous method with minor adjustment. SiNC was adsorbed nonspecifically to the surface of the Au NRs through electrostatic surface interactions and hydrophobic coordination with the present CTAB bilayer. Excess SiNC was added to ensure maximum adsorption of the PS. Stabilization with MHA-PEG, MUA-PEG, or MHDA-PEG followed shortly afterward, which bonded covalently to the surface of the Au NRs by formation of the moderately strong gold-sulfur bond. No chemical modification of SiNC was necessary as the coordination was based entirely on hydrophobic interactions, thereby eliminating the need to chemically alter the payload.

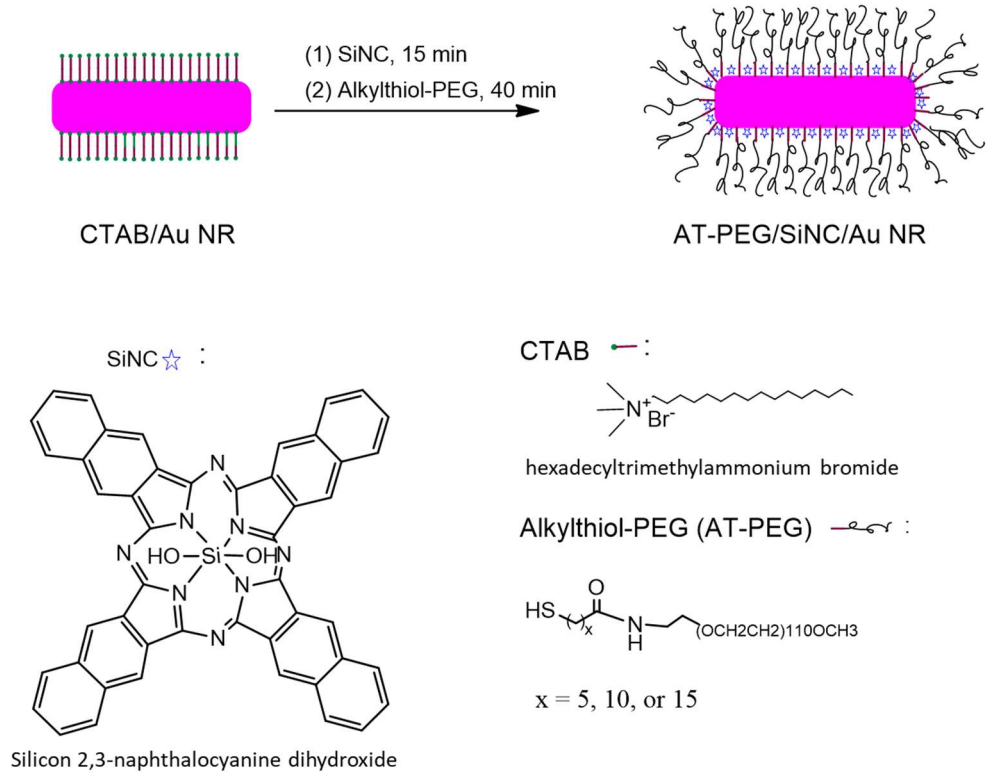

Figure 4.3: Schematic illustration of the preparation of AT-PEG/SiNC/Au NRs.

SiNC adsorption was characterized by Raman spectroscopy, which showed intense SERS signals of adsorbed SiNC on the nanocomplex, compared to uncoordinated SiNC in DMSO measured under the same conditions. Un-adsorbed SiNC was extracted from the nanocomplex assembly's supernatant left over during purification with DCM. The solvent was evaporated and SiNC re-dissolved in DMSO and measured by Raman Spectroscopy. Using quantitative measurements from a range of standard samples, the amount of SiNC left un-adsorbed was determined, thereby allowing the simple calculation of the number of SiNC molecules per Au NR in each of the three AT-PEG/SiNC/Au NR solutions. The results showed that MHA-PEG/Au NR attracted an average of 18,000 SiNC molecules to one nanorod, MUA-PEG/Au NR contained an average of 21,000 SiNC molecules per nanorod, and MHDA-PEG/Au NR contained

approximately 24,000 SiNC molecules per nanorod. Entrapment of molecules has been observed in other sources with an AT-tetra(ethylene glycol) system, and previously by Bhana *et al.* in loading paclitaxel onto Au NRs with MUA-PEG (5k).. It is believed that tight packing of AT-PEG on the NR surface allows the AT segment to form a hydrophobic pocket that traps and stabilizes the SiNC molecules close to the Au NR surface. Roughly 16% more SiNC is stored in MUA-PEG/Au NRs compared to the MHA- example, and roughly 33% more in the MHDA-PEG/Au NR complex. This demonstrates the significant effect of increasing AT chain length on increasing volume of loaded PS. It is believed that the hydrophilic PEG layer does not contribute significantly to SiNC coordination.

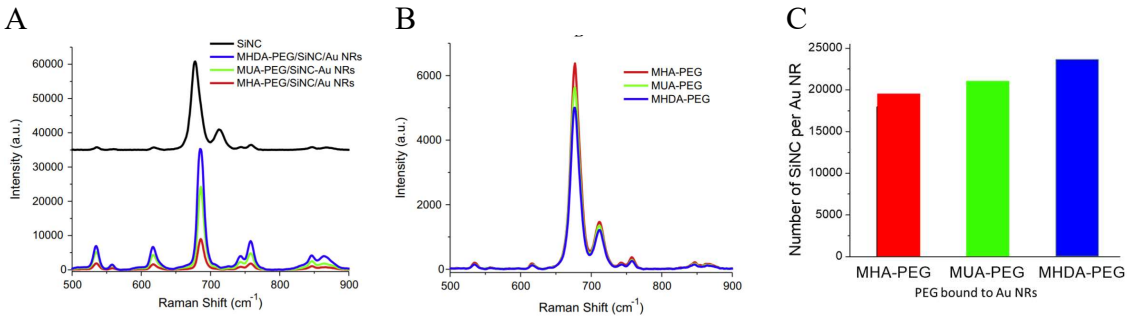

Figure 4.4: SERS spectra of AT-PEG/SiNC/Au NRs compared to the Raman spectrum of 1μM free SiNC. B) Raman spectra of un-adsorbed SiNC collected during the preparation of AT-PEG/SiNC/Au NRs. C) Quantitative display of the density of SiNC adsorbed on each Au NR determined from the free SiNC solution.

Finally, DLS demonstrated a notable size increase from 59nm NRs to 77, 79, and 82nm for MHA-PEG/SiNC/Au NRs, MUA-PEG/SiNC/Au NRs, and MHDA-PEG/SiNC/Au NRs respectively. Zeta potential changed from 31mV for as-prepared Au NRs to a slightly negative state for all three AT-PEG/SiNC/Au NRs, indicating the removal of the highly-positive CTAB layer and the presence of the mostly-neutral AT-PEG. Measurements of each complex without SiNC loading showed similar size and zeta

potential, which leads to the conclusion that the size increase and zeta potential change is solely due to the coordination of the AT-PEG to the Au NRs.

AT-PEG/SiNC/Au NRs Stability and SiNC Release. Stability of the AT-PEG/SiNC/Au NRs in physiological environments was done sequentially with in-vitro solutions that more closely replicate biological conditions. PBS, cell culture medium with 10% FBS, and 100% FBS were used, and the solutions were shaken continuously to replicate fluid motion. Samples of the AT-PEG/SiNC/Au NR solutions were collected at set times, centrifuged, and treated with DCM to extract the SiNC released from the nanocomplex. SiNC release was quantified by Raman spectroscopy after solvent evaporation and reconstitution in DMSO, as was done before. The results indicate a very slow pace of SiNC desorption. After one hour, no complex released more than 2% of bound SiNC. After 6h, just 8% of SiNC was released from any one compound. Alkyl chain length does not appreciably affect the percentage of SiNC release in any of these environments, though total molecular release will be higher for nanocomplexes with more SiNC loaded initially.

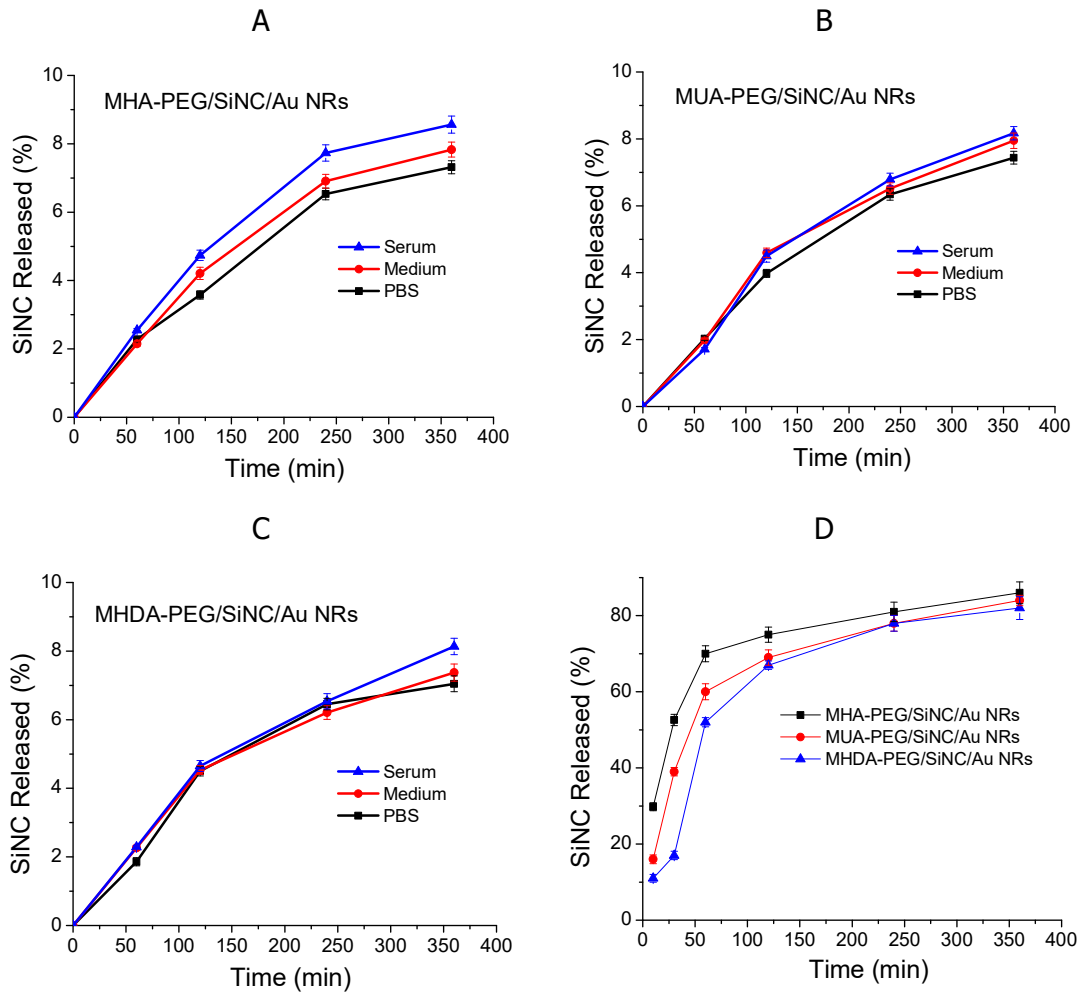

Figure 4.5: Stability of A) MHA-PEG/SiNC/Au NRs, B) MUA-PEG/SiNC/Au NRs, and C) MHDA-PEG/SiNC/Au NRs in PBS, cell culture medium, and serum. D) Comparison of the release of SiNC from AT-PEG/SiNC/Au NR complexes in the cellular environment.

Laser Irradiation and Cell Viability Measurement. The next immediate concern was delivery of the SiNC payload to cells. Hydrophobic molecules readily migrated to cells via partition between the surface of the nanocomplex and sites on the cell lipid membrane in Bhana, *et al.*'s work previously. It demonstrated a drug release mechanism augmented by exposure to cell surfaces. While this is a potentially negative quality for chemotherapeutics (which may be released to normal cells accidentally), it is a useful mechanism for PDT since localized light input will not activate PS molecules

incorporated into cells that are not in the target area. This effect on the AT-PEG/SiNC/Au NRs was explored by incubating three sets of KB-3-1 and SK-BR-3 cells with the appropriate cell culture medium containing one type of AT-PEG/SiNC/Au NRs each. Again, liquid-liquid extraction of the medium, collected at set times, determined the concentration of SiNC left in the medium. The release profile exhibits a two-phase system in which a large amount is released rapidly in a short window, followed by slower release over a long period of time. Release efficiency was dependent on AT identity: longer alkyl chains used in the nanocomplex resulted in slower PS release in the early, rapid phase. At 30 minutes, MHA-PEG/SiNC/Au NRs had released over 50% of its loaded SiNC, MUA-PEG/SiNC/Au NRs had released just 39%, and MHDA-PEG/SiNC/Au NRs released only 17%. However, at 6 hours, all three complexes had released about 80% of their payloads. Total SiNC delivered, therefore, was proportional to the amount first loaded onto each nanocomplex.

To effectively evaluate the capabilities of the AT-PEG/SiNC/Au NR nanocomplex for dual PDT/PTT therapy, we studied the cytotoxic effects of PDT, PTT, and PDT/PTT on KB-3-1 and SK-BR-3 cancer cell lines, representing two cancer types readily accessible by laser treatment. All three procedures were conducted with MHA-PEG/SiNC/Au NRs, MUA-PEG/SiNC/Au NRs, and MHDA-PEG/SiNC/Au NRs. PDT was conducted by adding an equivalent amount of SiNC as was released for the same incubation time from each of the complexes (as determined from the process above). PTT was accomplished using AT-PEG/Au NRs without SiNC loaded. Cells were incubated with medium infused with the specified treatment for two hours, and then irradiated with the 808nm laser for eight minutes. Cells were immediately washed with PBS to remove

the treatment solution and incubated in treatment-free medium overnight. XTT assay was used to determine the cell viability. Studies were carried out at the equivalents of three concentrations of nanocomplex (0.1nM, 0.3nM, and 0.5nM Au NRs) for both cell lines.

Statistical Analysis. Through statistical analysis with ANOVA and pair-wise comparisons using the Scheffe method, significant differences were found between the combined PDT/PTT treatment and the individual treatments for both cell lines using any of the AT-PEG/SiNC/Au NRs. For example, at 0.1nM concentration, the percent cell viability (XTT assay response over the response of the untreated control) for MHA-PEG/SiNC/Au NRs was 17.3% for KB-3-1 cells and 18.3% for SK-BR-3 cells. The equivalent PDT treatment (SiNC only) retained a 58.4% viability for KB-3-1 cells and 59.9% viability for SK-BR-3 cells. PTT at equivalent concentration showed 40.7% cell viability for KB-3-1 cells and 33.8% viability for SK-BR-3 cells. Thus, the dual treatment managed to kill ~41% more cells compared to PDT and between 15 and 23% more cells than PTT alone. This shows that combined PTT and PDT is significantly more effective than either treatment alone; this pattern was also observed in treatments involving MUA-PEG and MHDA-PEG as the stabilizing agents. Between the three alkyl chain lengths on the AT-PEG/SiNC/Au NRs, the longest chain, MHDA-PEG/SiNC/Au NRs, showed a higher cell killing efficiency than the shorter chains. Given the same release efficiency but greater SiNC loading, MHDA-PEG/SiNC/Au NRs' improved killing efficiency is attributed to the greater presence of SiNC delivered to the cells.

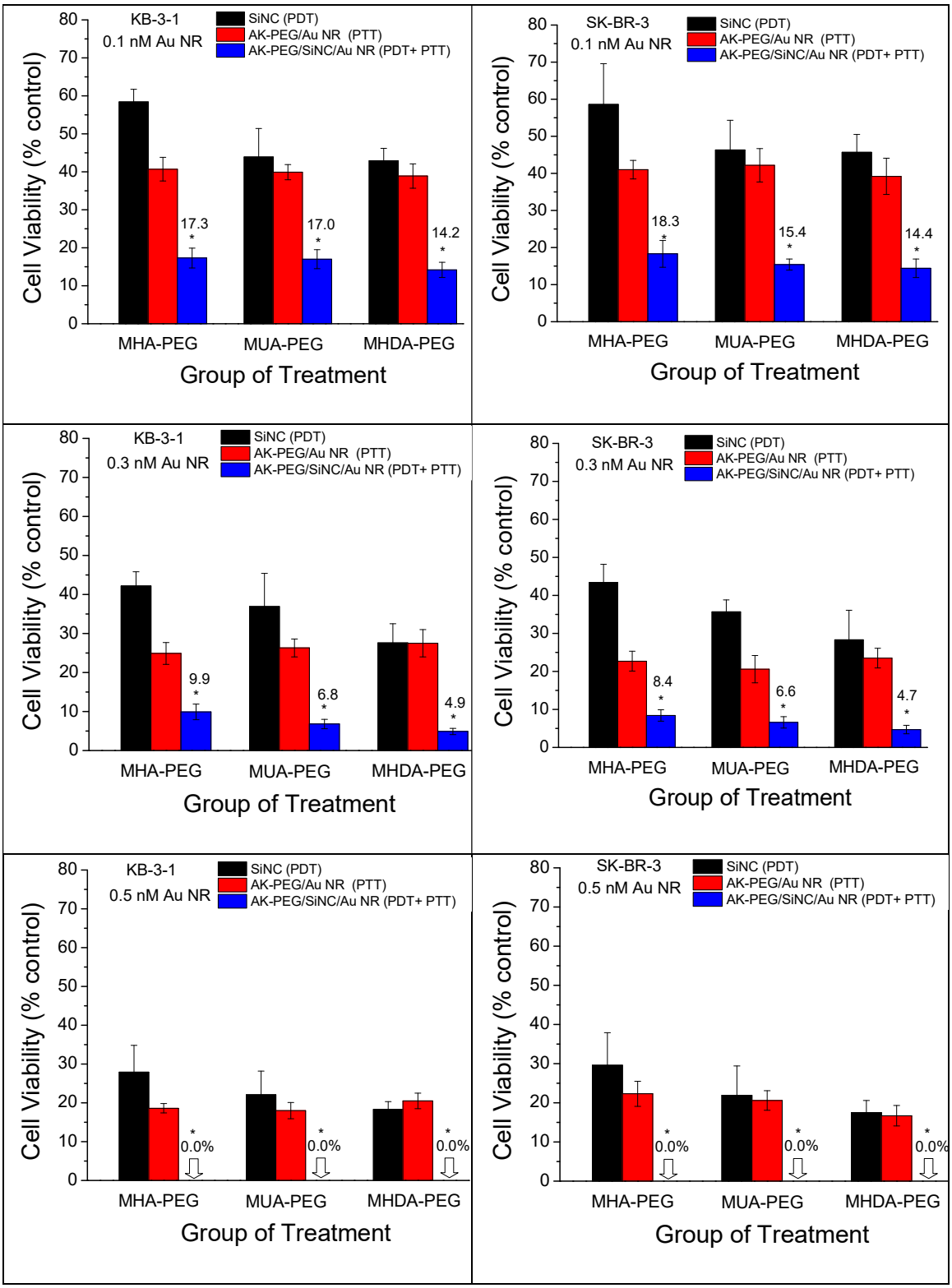

Figure 4.6: Comparison of the efficacies of PDT and PTT with AT-PEG/SiNC/Au NRs using KB-3-1 (left) and SK-BR-3 (right) cells at different doses to that of PDT (free SiNC) and PTT (with mPEG/Au NRs) at equivalent concentrations.

Increasing concentration led to increased cell death for all treatments. For example, increasing the concentration of MHA-PEG/SiNC/Au NRs from 0.1nM to 0.3nm decreased the average cell viability from 14.2% to a mere 4.9% for KB-3-1 cells, with similar reduction observed for SK-BR-3 cells. Further increase in concentration for all three complexes led to outright destruction of cells in the well. Increasing the concentration not only increased the presence of SiNC in solution, but also the heating of the medium itself, as seen from the characterization of Au NRs. Thus, increasing the concentration positively effects both methods of treatment, as demonstrated by the complete eradication of cells by all three nanocomplexes.

It was hypothesized that elevated temperature due to photothermal effect may increase cell membrane permeability, both to photosensitizer incorporation and vulnerability to reactive oxygen species yielded by the same. Such alteration may result in a synergistic effect between PDT and PTT. To detect whether a potential synergistic effect exists in our treatment method, compared to a simple additive method, cell viability was compared between the two independent methods and the combined therapy to see if significant differences exist. The relationship used was $f_{additive} = f_{pdt} \times f_{ptt}$[101], where $f_{additive}$ is the additive fraction of cells surviving that would result from a theoretical dual treatment with no interaction, f_{pdt} is the fraction of surviving cells resulting from PDT, and fptt is the fraction of surviving cells from PTT. This was calculated for each alkyl chain length used, and each concentration. If we consider the dual PDT/PTT result to be $f_{combination}$, or the fraction of surviving cells undergoing the observed simultaneous therapy, then we can compare $f_{additive}$ to $f_{combination}$. When $f_{combination}$ is observed to be higher than $f_{additive}$, then more cells are surviving than should be, theoretically, if both

treatments have no interaction, thus the two treatments are antagonistic. If $f_{combination}$ is observed to be lower than $f_{additive}$, however, then the effects are synergistic and causing more cell destruction than the theoretical non-interfering example. From our calculations, we clearly see an observed surviving fraction that is consistently lower than the theoretical $f_{additive}$ for each concentration and alkyl chain length. Thus, we see strong evidence that the dual PDT/PTT therapy is synergistic in nature.

Table 4.1: Comparison of calculated $f_{additive}$ with experimental $f_{combination}$ between PDT and PTT for KB-3-1 and SK-BR-3 cells.

		KB-3-1		SK-BR-3	
Nanocomplex	**Concentration (nM)**	$f_{additive}$	$f_{combination}$	$f_{additive}$	$f_{combination}$
MHA-PEG/SiNC/Au NRs	**0.1**	**23.8**	**17.3**	**24.1**	**18.3**
	0.3	**10.5**	**9.9**	**9.8**	**8.4**
	0.5	**5.2**	**0**	**6.6**	**0**
MUA-PEG/SiNC/Au NRs	**0.1**	**17.5**	**17.0**	**19.5**	**15.4**
	0.3	**9.7**	**6.8**	**7.4**	**6.6**
	0.5	**3.9**	**0**	**4.5**	**0**
MHDA-PEG/SiNC/Au NRs	**0.1**	**16.7**	**14.2**	**17.9**	**14.4**
	0.3	**7.6**	**4.9**	**6.7**	**4.7**
	0.5	**3.7**	**0**	**2.9**	**0**

Conclusion

Simultaneous PDT and PTT carried out with NIR laser irradiation serves to maximize the effectiveness of cancer phototherapy. We have produced an improvement on the design of the PS-Au NR nanocomplex design. We used the photosensitizer SiNC, which possesses a high singlet oxygen species yield and optimal absorption spectrum for PDT in biological condition, and we developed an AT-PEG/Au NR that can be deliver the PS by the tens of thousands per carrier vehicle by incorporating the molecule into a hydrophobic pocket for transport. Stabilized against influence by biological sources by

the PEG outer layer, this nanocomplex will have a long circulation time in-vivo which will ensure collection at the relevant tumor sites for release of SiNC and eventual laser application.

We hypothesized that the AT-PEG/SiNC/Au NR complex allows for dual PDT/PTT under a single laser irradiation and that increasing chain length would increase therapeutic response and tested these with two cancer cell lines of differing origins. We demonstrated that combining PDT and PTT was possible and produced notable effects above and beyond the predicted result of either treatment alone. Comparative studies between three AT chain lengths (MHA, MUA, and MHDA) demonstrated that the cytotoxicity increased as chain length increased, due to the increased SiNC loading efficiency. Cell killing efficiency was also found to be dose dependent, with higher percentages of cell death incurred as concentration increased, right up to complete cell eradication by low-power laser irradiation.

Future exploration of this capability will investigate the effects of AT chain length on in-vivo conditions, such as biodistribution and delivery efficiency into tumor sites. This will establish the most optimal chain length for continued study towards developing a tumor therapy technique. Additionally, the incorporation of some type of targeting method should be investigated. We envision that targeted delivery of MHDA-PEG/SiNC/Au NRs will be able to ablate tumors with high effectiveness, to degrees that will significantly decrease the probability of tumor regrowth and metastasis. Such a methodology would be a notable tool to add to the range of treatment options for breast cancer, head and neck cancer, and other light-accessible cancer types.

Chapter 5

Isolation, Detection, and Analysis of Circulating Tumor Cells Using Iron Oxide-gold Core-shell Nanoparticles

Introduction

As described in the literature review, circulating tumor cells (CTCs) are malignant cells that have shed from a primary tumor into the bloodstream of a cancer patient[74]. CTCs embed elsewhere in the body to become a locus for the formation of new tumors within the patient; the presence and number of CTCs in blood is a trademark characteristic of metastatic behavior[76]. Since complications from metastasis are the cause of 90% of cancer-related deaths, the study of CTCs is paramount to aiding the advancement of treatment in the most dangerous cancer types[102]. CTCs have been detected in early stages of tumorigenesis, even before the origin tumor was detectable by modern imaging equipment[76]. The capture and profiling of CTCs provides a unique opportunity for the detection of early metastasis, prognosis evaluation, therapy targeting, and treatment effectiveness evaluation[78,79,80].

CTC detection is challenging due to two major obstacles. First, CTCs are exceptionally rare in the bloodstream. In one milliliter, five billion red blood cells and ten million white blood cells must be sifted through to find as few as one CTC. Second, CTCs share much in common with their parent tumor, however tumor populations have some degree of heterogeneity and tumor cells undergo some adaptation when passing from the epithelium into the blood stream[76]. Capture techniques therefore require extremely specific and sensitive techniques to isolate CTCs with high efficiency. Multiple techniques have been developed over the last twenty years that have vastly

improved CTC detection, however only one technique, the CellSearch system by Veridex, LLC, is approved by the United States Food and Drug Administration (FDA) [77]. This system characterizes the most common approach to CTC detection: initial isolation of CTCs, then enrichment and analysis based on biomarker expression. CellSearch's immunomagnetic separation technique isolates CTCs, however the magnetic beads are targeted only against EpCAM, a marker that only tests positive in 50-70% of metastatic cancer patients, therefore this system limits its ability to detect more diverse cancer types that do not express this surface marker. Additionally, the procedure involves many preparation steps and long turnaround times[84,103]. This increases procedural cost and the likelihood of sample decay or loss.

Dye-adsorbed metal nanoparticles (NPs) that rely on surface-enhanced Raman scattering (SERS) emerged as a new label for biological samples. SERS NPs circumvent the rarity of Raman scattering and allow for extremely sensitive detection and specificity compared to traditional immunofluorescent detection. Additionally, SERS produces spectra with fingerprint peaks tens of times narrower than that of fluorescence and not subjected to autofluorescence, giving SERS an advantage in precise molecular detection with potential to detect multiple dyes simultaneously.

We have reported previous research demonstrating an assay for highly-sensitive detection of epithelial cancer cells in whole blood using dual-function magnetic-optical iron oxide-gold (IO-Au) core-shell nanoparticles. These hybrid nanoparticles combined superparamagnetic properties of the iron oxide core with an optically active oval-shaped gold shell. When immunotargeted, these nanoparticles selectively separated cancer cells from whole blood by flowing the sample through a one-channel capillary tube across an

external magnet. IO-Au SERS NP-labeled CTCs were pulled down and captured by this magnet and the capture area was analyzed by Raman Spectroscopy. Cells were captured with 95% efficiency and the limit of detection was found to be 1-2 cells/mL, an exceptional step forward in both sensitivity, rapidity, and simplicity of sample processing[92]. This system remains limited, however, in the capacity to differentiate multiple biomarkers and cannot perform single-cell analysis.

We report the development of a new system using multiplexed, multicolor Raman-coded IO-Au NPs to identify, magnetically capture, and analyze CTCs in whole blood with a SERS microscope and microfluidic device. This system carries over the dual isolation and detection nanoparticle scheme from the previous assay and increases its usefulness in three distinct ways. First, multiplexed detection allows for a wide range of markers to be used, vastly broadening the types of CTCs that will be captured and increasing detection sensitivity. Second, captured CTCs can be analyzed for these biomarkers under a single excitation event simultaneously on a single-cell basis without need for complicated signal processing and absent of autofluorescence and photobleaching. Third, all processes take place on a microfluidic device that is adaptable for automation, thus increasing the repeatability and ease of integration into a clinical setting. This method has the potential to make a notable clinical impact through more reliable detection of CTCs and ability to inform treatment options by providing surface protein profiles, thereby enhancing the personalization of cancer treatment. We demonstrate this capability with a four-target system involving four dye-adsorbed IO-Au NPs with four separate antibodies targeting known cancer surface markers (EpCAM,

HER2, CD44, and IGF-1R). This system can be easily adapted to many other fields such as the detection and identification of pathogens.

Experimental Methods

Synthesis and Characterization of Iron oxide-Gold Core-shell Nanopopcorn. Iron-oxide gold nanoparticles were synthesized according to the methods reported in Kwizera, *et al.*[94] as a development of the seed-mediated growth method. First, octahedral iron oxide core nanoparticles were synthesized via a modification of the method by reported by Goon *et al.*[104] Briefly, 175mg of iron sulfate ($FeSO_4$), 2.5mL of 2.0M potassium nitrate (KNO_3), 2.5mL of 1.0M sodium hydroxide (NaOH), and 5mL of 8mg/mL polyethyleneimine (PEI branched, approx. 25,000 MW) were added to 20mL of ultrapure water purged with nitrogen. In an oxygen-free environment, the mixture was heated to 90° C under vigorous stirring, with continued heating at this temperature for two hours. During the heating process, the solution changed color from blue to black, indicating the formation of iron oxide nanoparticles. The nanoparticles were purified by magnetic separation five times and then redispersed in 20 mL of ultrapure water.

Once again, the method by Goon *et al*. was modified to grow core-shell nanoparticles. Au seeds were attached to IO NPs to facilitate the growth of Au shell. Firstly, small Au NPs were synthesized by the reduction of chloroauric acid (HAuCl4, 2 mM) with sodium borohydride (0.2M) in the presence of sodium citrate (0.85 mM). These were then attached to PEI-stabilized iron-oxide nanoparticles via electrostatic interactions between the polymer stabilizer and the charged Au surface. 55µL of 0.32mg (Fe) PEI-stabilized IO NPs were added to 5 mL of as-prepared Au NPs and stirred for 45min. After purification by three cycles of magnetic separation and washing, the

solution was redispersed in 2.5mL of 15mg/mL PEI aqueous solution and heated at 60ºC for 3 hr. After purification by three cycles of magnetic separation and washing, the seeds NPs were redispersed in 1mL of ultrapure water.

To make IO-Au core-shell NPCs, an Au growth solution was prepared by adding 200µL of 10mM HAuCl4 into a 5mL solution of 0.1M cetyltrimethylammonium bromide (CTAB) aqueous solution. After mixing for 5 min 30 µL of 10 mM silver nitrate ($AgNO_3$) was added and stirred for five minutes before 90µL of 100mM ascorbic acid (AA) was added to reduce $HAuCl_4$ to $HAuCl_2$. Then, 150µL of gold-seeded iron oxide nanoparticles from the prior step was added. The solution was stirred for ten seconds, followed by undisturbed incubation for two hours in a 25ºC water bath to allow complete growth of IO-Au core-shell nanopopcorn. Purified products of these steps were analyzed with nanoparticle tracking analysis and transmission electron microscopy.

Synthesis of Multiplexed Antibody-targeted SERS Nanopopcorn. First, 5µg of antibody was washed with PBS and then mixed with 5µL or 10µL of 1mM NHS-PEG-SH (MW 5000) to be incubated at 4ºC overnight. Next, the solution was purified and washed three times by 10,000MW centrifuge filtration and reconstituted in 20µL deionized water. This was then added to 50µL of 50pM IO-Au NPCs and mixed in the dark for 8 hours at room temperature. Next, 10µL of 100uM QSY-21, (20,000:1), was added and stirred in for five minutes. 25µL of 1mM MHDA-PEG (MW 5000) was then added to the solution and stirred for ten minutes, at which time the NPC solution was purified by centrifugation (10,000rpm, 10 minutes) and re-dispersed in 250µL of PBS (50pM final concentration). Surface modifications were measured at each step by size of

the nanoparticles collected via nanoparticle tracking analysis and zeta potential determined by dynamic light scattering.

Construction of an Integrated Microfluidic Chip for Cell Isolation, Detection, and Profiling. The microfluidic chip was designed to include a wide, shallow, flat channel for efficient cellular capture in the center, and optically transparent for detection and profiling. This was balanced with producing a laminar flow across the capture field while allowing for high fluid throughput. The resulting chip (manufactured by Micronit Microfluidics) was made of two 45mm x 15mm x 1mm quartz slides. One slide was etched with 100µm-deep channels and the other contained the 1mm input and output channels to feed fluid to and from the device after fusion. The isolation and detection chamber was etched to a dimension of 20mm x 5mm x 0.1mm with six fluid ports feeding to this chamber. Five ports enter through one side via a merged channel and the other has a single outlet channel. Capillary tubes are attached to all six ports, with the five inlet tubes attached to syringes that feed their respective solutions into the channel. For manual experimentation, only the center tube was used for all products. A removable magnet fixed in a Styrofoam holder is placed underneath the central chamber to isolate the targeted cells but allow for analysis by microscopic means. This device is placed on the stage of an Olympus combination fluorescence and Raman microscope with variable objectives. Construction parameters are shown in Figure 5.4 B-C.

Cell Culture Protocol and Cell Labeling with Antibody-conjugated IO-Au SERS NPCs. Human breast cancer cells SK-BR-3, MCF-7, MDA-MB-468, and MDA-MB-231 were cultured in appropriate media (RPMI 1640 with 10% fetal bovine serum for SK-BR-3 and DMEM with 10% fetal bovine serum for MCF-7, MDA-MB-468, and

MDA-MB-231) under 5% CO2 at 37oC. To label cells with antibody-conjugated IO-Au SERS NPCs, approximately 300,000 cells in 100μL of PBS were incubated with 10μL of 50pM IO-Au SERS NPCs for 30 minutes at 37oC with occasional stirring to keep cells suspended. Multiplex labeling was carried out using 10μL of each individual particle population. The cells were purified by repeated centrifugation and washing (1500 rpm, 3 min). IO-Au SERS NPCs conjugated with rabbit IgG were used as the control. Cells were fixed with 4% paraformaldehyde and cellular binding was observed with dark field microscopy with an Olympus IX71 inverted microscope.

Determination of Capture Efficiency. Optimization of the flow rate to maximize capture efficiency of cells while minimizing free particle capture in the magnetic region of the microfluidic chip was carried using SK-BR-3 cells labeled with a cocktail of all four antibody-targeted IO-Au SERS NPCs, of which anti-EpCAM and anti-HER2 have a high affinity. 1mL of 300,000 prelabeled, fixed cancer cells were pumped through the microfluidic chip at a range of flow rates, and the solution collected at the end. Uncaptured cells in the collected solution were counted by hemocytometer to determine capture efficiency of labeled cells. To determine the capture efficiency of free IO-Au NPCs, 1mL of 5pM MHDA-PEG-stabilized IO-Au NPCs were flowed through the microfluidic chip under the presence of the magnet at various flow velocities and collected at the end. Uncaptured NPCs were quantified by UV-Vis absorption spectroscopy. Capture efficiency of both NPs and cells were expressed as percentages of the starting solution concentration and cell count, respectively.

Molecular Profiling of Cells with Single-Color IO-Au SERS NPCs. Each cell line was tested individually against QSY-21-tagged IO-Au SERS NPCs conjugated to

either anti-EpCAM, anti-HER2, anti-CD44, or anti-IGF-1R. Cells were labeled as described above with a single particle type, fixed, and re-dispersed to a volume of 20µL, and deposited on a quartz microscope slide. Raman spectra of 50 individual cells were collected at 40x zoom with the Raman microscope (spot size ~20um, 25mW, 30s integration time). The appropriate antibody-IO-Au SERS NPCs were measured at 5pM as a standard. Cell expression was quantified as an average maximum signal of these 50 cells. To make each individual profiling comparable with the others, the standard solution spectra were normalized to a maximum of 1,000 counts, and the normalization factor applied to the average signal of each population. Molecular profiles of each cell line was verified by flow cytometry.

Molecular Profiling of Cells with Multicolor IO-Au SERS NPCs. Each cell line was tested individually against four-color IO-Au SERS NPCs, labeled with QSY-21, BHQ-3 amine, QXL-680, and 740 dye, and conjugated to anti-EpCAM, anti-HER2, anti-CD44, and anti-IGF-1R respectively. Cells were labeled as described above with an equal amount of all four particle types, fixed, and re-dispersed in a volume of 20µL deposited on a quartz microscope slide. Raman spectra of 50 individual cells were collected at 40x zoom with the Raman microscope as described above. Raman spectra were also taken from the four particle solutions for use as pure standards. The signals were processed using (Eigenvector) software by conducting classical least squares (CLS) regression. Spectra from the particle solutions, along with a background signal gathered at the time of signal collection, were inputted to generate a software model. Spectra of the labeled cells were then analyzed with this model and the output gathered.

Detection and Molecular Profiling of Cells with Multicolor IO-Au SERS NPCS in PBS and Whole Blood. 1mL of PBS or human whole blood was spiked with 100-1,000 SK-BR-3 cells. 100µL of 50pM IO-Au SERS NPCs of each dye-antibody pair were added, and then the solution was incubated for 30 mins at 37^{o}C and periodic mixing to keep cells dispersed. PBS or whole blood without spiked cancer cells was used as the control. The solution was flowed across the microfluidic device in the presence of the magnet. PBS was flowed through afterwards at a slower rate to wash the captured cells, followed by a wash of DAPI and FiTC-anti-CD45 to stain the cells. Finally, the cells were fixed by flowing 4% paraformaldehyde across the chip. Cells were then analyzed using fluorescence microscopy to locate nuclear cells and eliminate CD45+ white blood cells. 50 cells were analyzed to verify profiling efficacy and total cell counts were conducted to determine capture efficiency. As previously stated, SERS spectra were collected of the IO-Au SERS NPCs and entered to generate a CLS model and deconvolute the spectra of the cells.

Results and Discussion

Synthesis and Characterization of Iron oxide-Gold Core-shell Nanopopcorn. Previous publications have taken advantage of the effect of anisotropy in particle shape to enhance the electric field surrounding a plasmonic nanoparticle. Raman scattering of nearby dye molecules is boosted by the fourth power of the electric field, meaning that a small increase in local electric field can lead to immense gain in Raman signal. Therefore, given a population of differently-shaped particles of equal size, anisotropic particles prove better substrates compared to spherical designs. Kwizera *et al.* produced a wide range of particle shapes that allow for various anisotropic characteristics, and these

were considered as candidates for this project. Eventually, 85nm nanopopcorn were chosen as the best candidate due to a balance between SERS intensity, (still over ten times that of 85nm spherical core-shell nanoparticles), shell thickness, to maintain strong magnetic properties, and surface morphology for effective antibody conjugation. 75nm nanostars demonstrated the greatest SERS promise but the large tips and deep valleys of the particle surface reduced the effective antibody conjugation population to only those which were linked by chance to the tips. Additionally, 85nm NPCs presented superior magnetic separation characteristics relative to larger sizes.

The synthesis and characteristics of 85nm NPCs are detailed in Figure 5.1, which displays the uniform octahedral cores, thorough seed coating, and monodisperse character of the final product. Absorption was broadly between 500 and 800nm, with a maximum between 650 and 700nm.

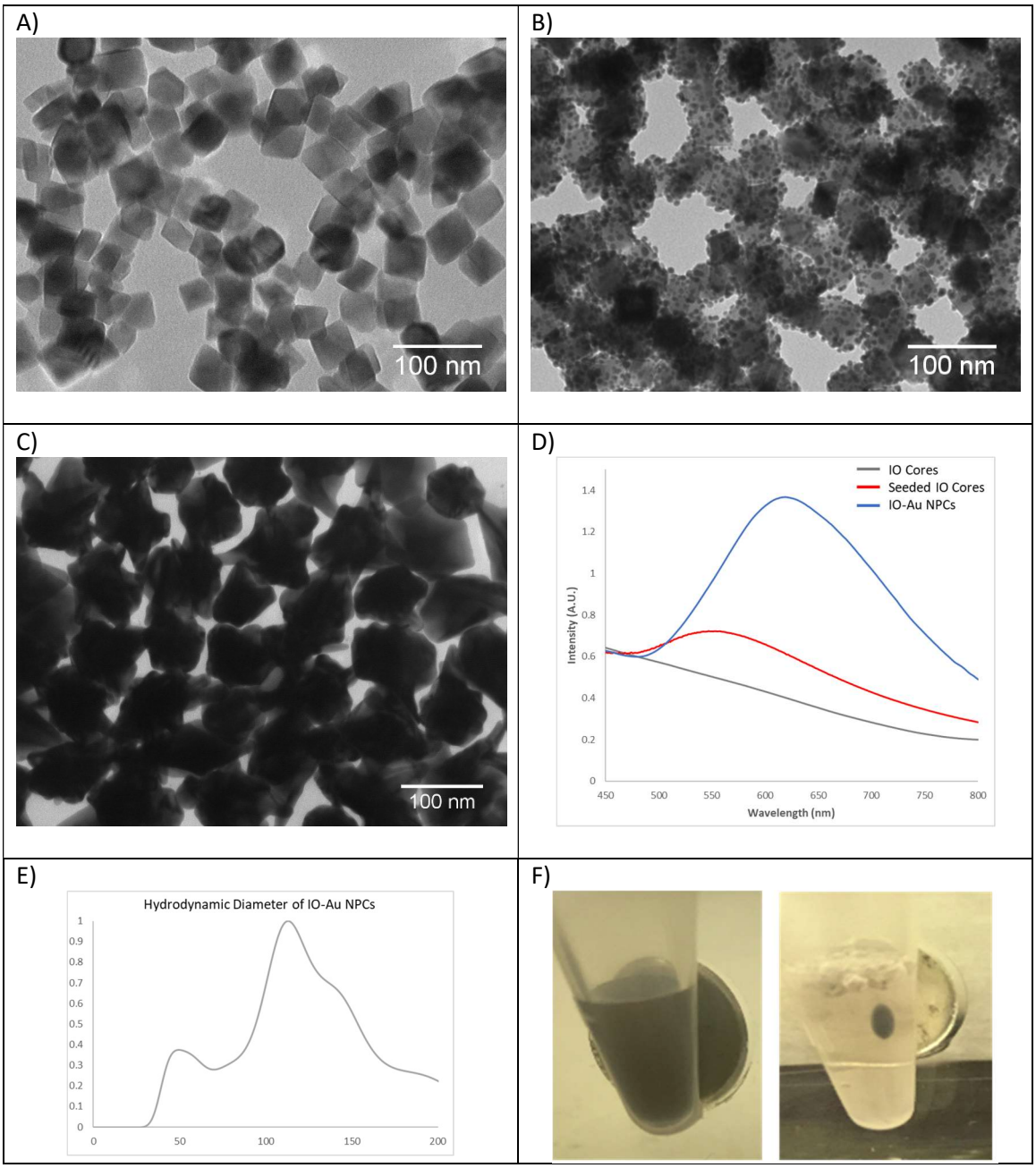

Figure 5.1: Characterization of iron oxide and iron oxide-gold core-shell nanopopcorn. A) TEM image of IO NPs. B) TEM image of IO NPs seeded with Au NPs. C) TEM images of IO-Au NPCs. Average central size is 85nm. D) UV/Vis absorption spectra of IO NPs and IO-Au core-shell NPCs. E) Size analysis of IO-Au NPCs collected by Nanoparticle Tracking Analysis. Average hydrodynamic diameter was 127nm. F) IO-Au NPCs before and after magnetic separation in under four hours.

Cell Culture Protocol and Cell Labeling with Antibody-conjugated IO-Au SERS NPCs. We chose a range of breast cancer lines as a model for this proof-of-concept, including the aggressive cancer line MDA-MB-231. Antibodies were first chosen due to their commonality in cell lines and selective absence. Epithelial cell adhesion molecule (EpCAM) was included as the standard capture marker for epithelial cancers, as used on the CellSearch system. Human epidermal growth factor receptor-2 (HER2) is a marker known to be overexpressed in 30% of breast cancers[105]. CD44 is a surface protein associated with cell adhesion and migration, and often overexpressed in cancer stem cells. Insulin-like growth factor-1 receptor (IGF-1R) is a transmembrane receptor that is implicated in metastatic progression of certain breast cancers.

The desired Antibodies were linked to a thiol-PEG by a carbodiimide coupling reaction, which was conducted at neutral pH and left overnight at cold temperature to control the rate of NHS hydrolysis. The linked antibody-PEG-SH was washed by centrifuge filtration to dispose of excess PEG and re-disperse the antibody in water. The antibody-PEG-SH was then bound to the surface of the nanoparticle by covalent bonding of the sulfur to the gold surface. DLS revealed the binding of antibody to the particle by a change of hydrodynamic size by ~10nm and a zeta potential decrease as the positively-charged CTAB layer was displaced. After eight hours of gentle stirring, the Raman reporters were added to the solution, which bound electrostatically to the surface of the particles in solution. This binding does not appreciably change the hydrodynamic diameter or zeta potential of the particles but is verifiable by Raman spectroscopy of the solution. The Raman dyes were chosen due to their limited overlap with one another, their relative ease of binding to nanoparticles in water, and their long-term stability.

Finally, the dye-adsorbed antibody-conjugated NPCs were stabilized by application of MHDA-PEG, which bound to the surface by the gold-sulfur bond on the alkyl chain. MHDA-PEG was chosen for its superior ability to stabilize the Raman reporters on NPs compared to methyl-PEG alone. The hydrophobic pocket formed near the surface of the nanoparticle likely stabilizes the weakly-soluble dye molecules in a position near the nanoparticle, thus maintaining their SERS activity for longer in complex environments and conditions, such as those incurred by the cell labeling process. Particle hydrodynamic size increases again by ~30nm and zeta potential is measured as weakly negative.

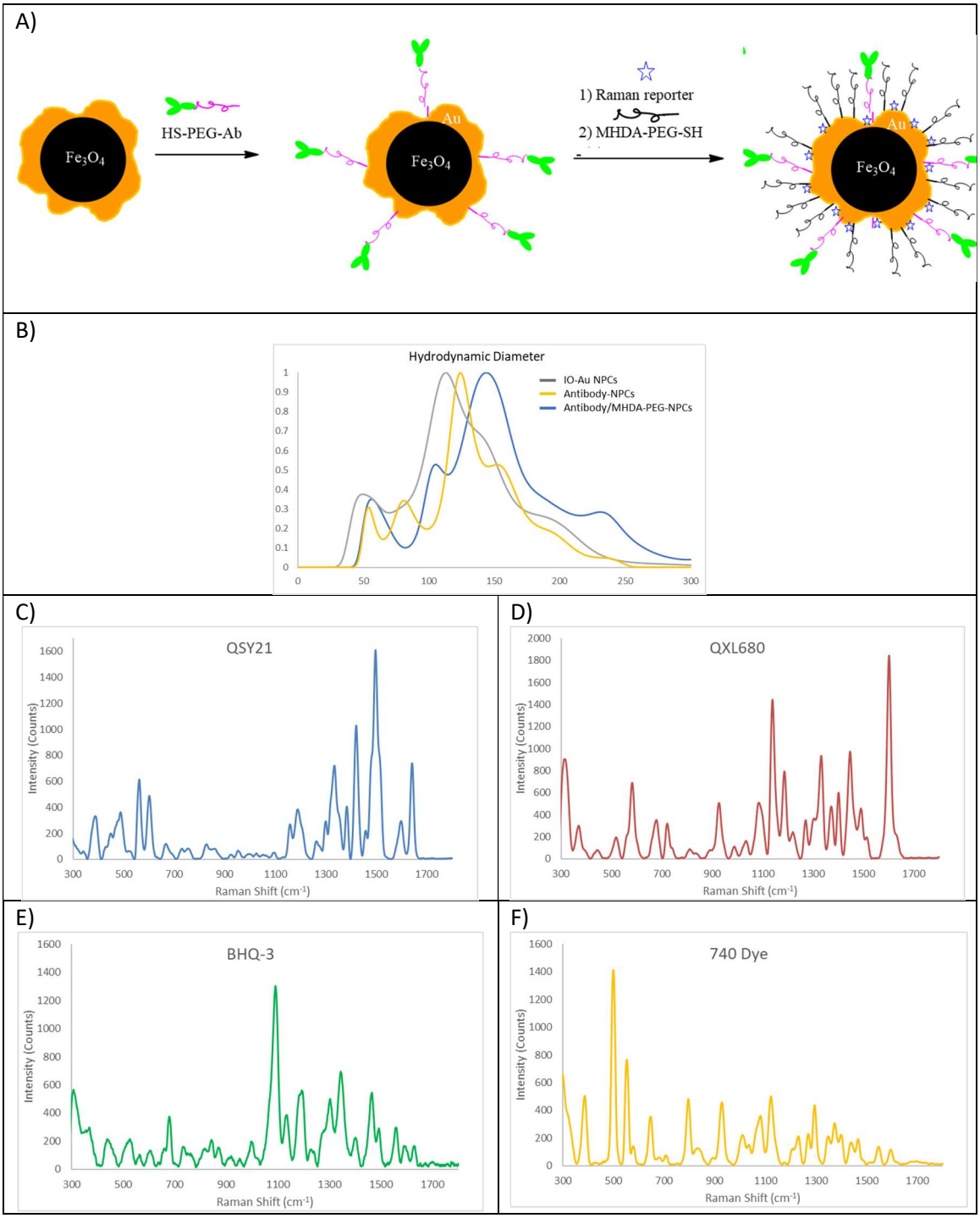

Figure 5.2: A) Schematic of preparation of SERS-Active IO-Au core-shell NPCs targeted to different cancer cell markers. B) Size analysis of IO-Au SERS NPCs before and after antibody conjugation collected by nanoparticle tracking analysis. Sizes were 127nm, 130.4nm, and 162nm respectively. C-F) SERS spectra of IO-Au NPCs adsorbed with Raman Reporters QSY-21, 740 Dye, QXL-680, and BHQ-3-NH_3.

Cancer cell labeling was conducted by incubating 300,000 cells in 100µL with 10µL aliquot of 50pM of one type of IO-Au SERS NPCs, producing a roughly 5pM final concentration of that NPC type. Multiplex experiments did not change individual particle concentrations; total NPC concentration in a multiplex experiment was 20pM, made up of 5pM of each antibody-dye paired NPC. Dark field imaging verified the successful conjugation of each nanoparticle type, with dense particle presence on the cell surface confirming successful binding, as shown in Figure 5.3. This was also used to qualitatively profile the cell lines with the SERS NPs, verifying the selectivity and rarity of nonspecific binding. The surface marker expressions of each cell line was matched against flow cytometry of these cell lines gathered while pursuing a different publication for confirmation.

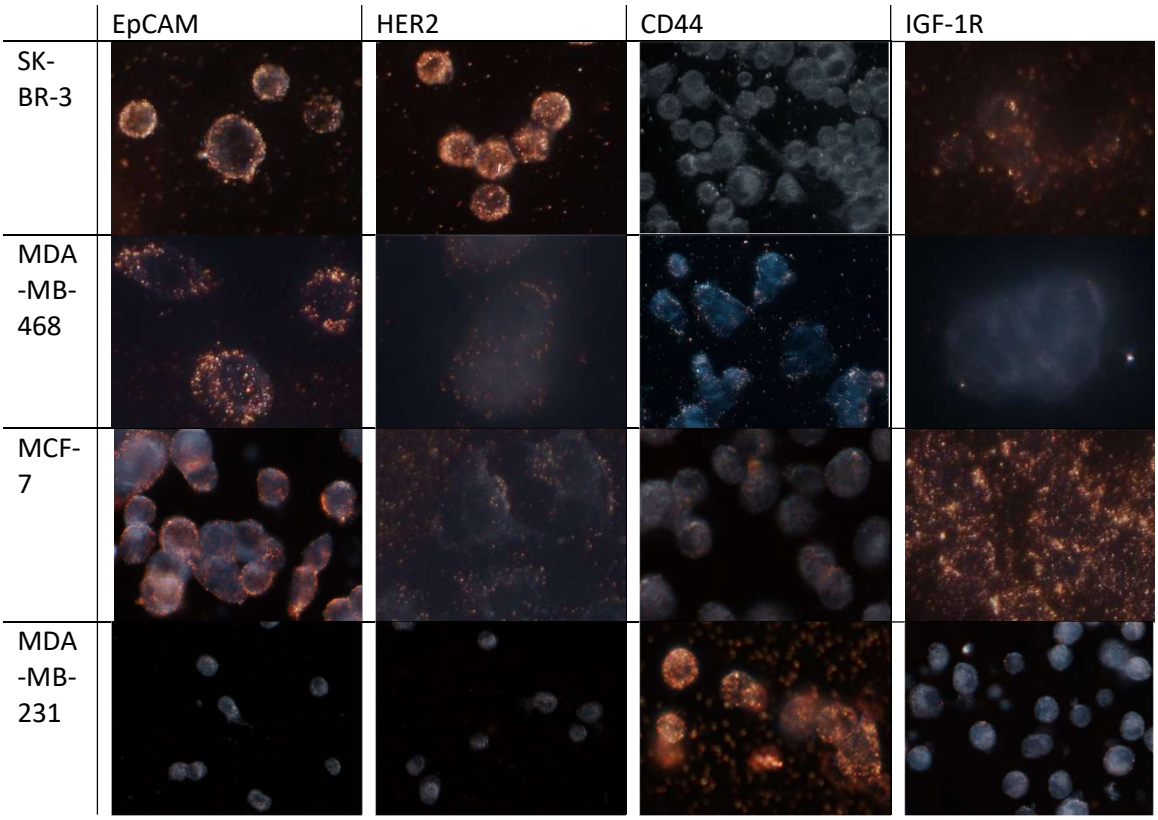

Figure 5.3: Dark field microscopy of breast cancer cell lines SK-BR-3, MDA-MB-468, MCF-7, and MDA-MB-231 after 2h incubation at 4°C with IO-Au NPCs coated with QSY-21, QXL-680, BHQ-3-NH_3, and 740 Dye*, conjugated with anti-EpCAM, anti-HER-2, anti-CD44, and anti-IGF-1R respectively.

Determination of the Capture Efficiency of the Microfluidic Device. Results of the capture percentages of both IO-Au NPCs and labeled cells are given in Figure 5.4 D. Capture efficiency of labeled cells was found to be approximately 95% at 1-5µL/min but decreased dramatically from 200µL/min (88%) to 300µL/min (40%). Free IO-Au NPC capture was found to have an increasing capture efficiency at any rate lower than 100µL/min. Unlabeled cells were captured at less than 10% at any flow rate tested. To optimize cell uptake, sample throughput, and limit the capture of free SERS NPCs, a flow rate of 200µL/min was chosen for the capture and separation of CTCs from whole blood components.

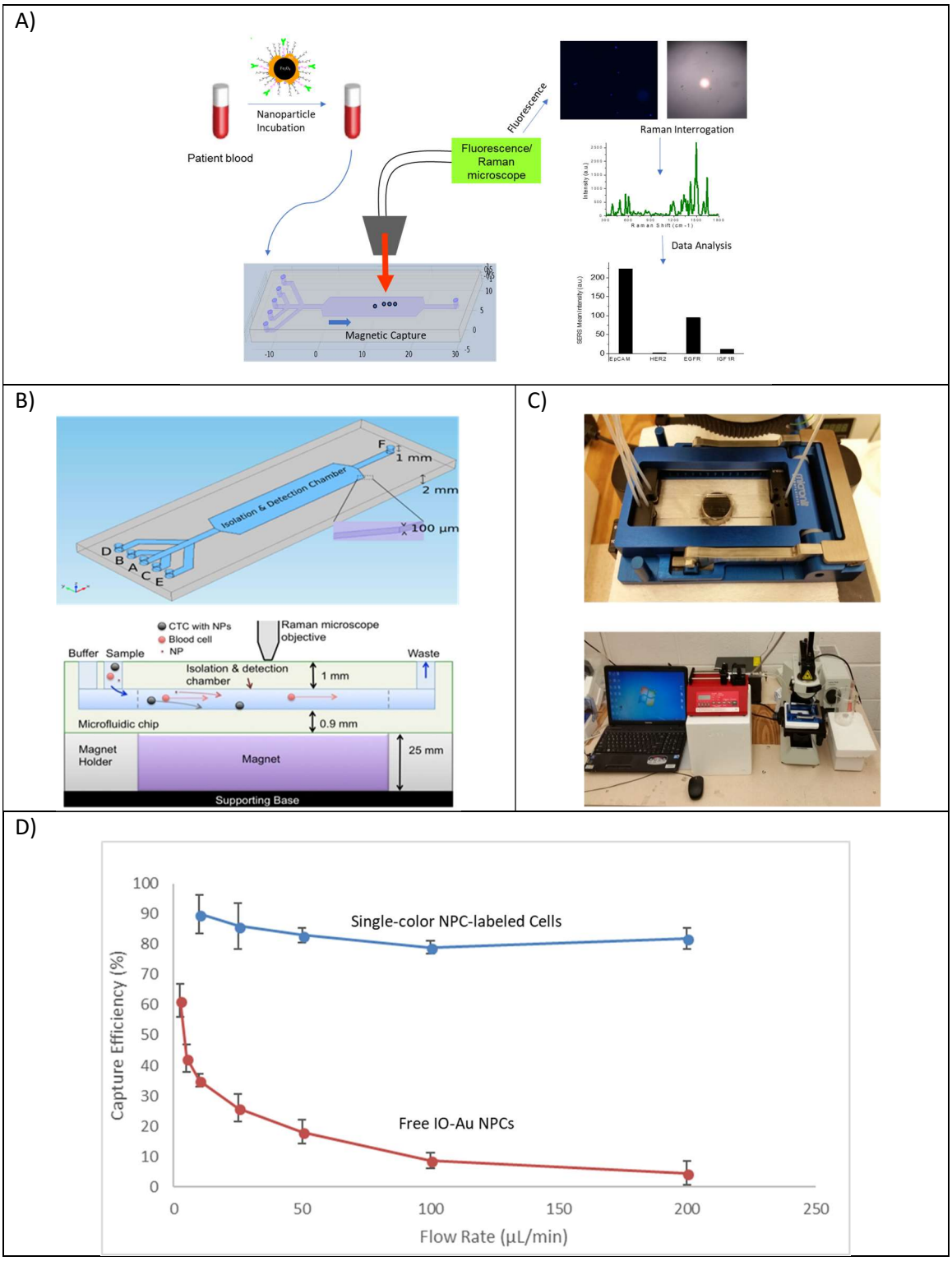

Figure 5.4: A) Schematic of whole blood sample preparation for magnetic separation and SERS detection of CTCs. B) Schematic of the microfluidic device for on-line CTC separation, detection, and analysis. C) Photographs of the microfluidic device and instrument setup. D) Capture efficiency of free NPCs and SK-BR-3 cells labeled with anti-EpCAM conjugates.

Molecular Profiling of Cells with Single-Color IO-Au SERS NPCs. To confirm the profiling capability of the IO-Au SERS NPCs and to set a comparable baseline for future profiling reliant on deconvolution, a single dye, the fluorescence quencher QSY-21, was chosen to conduct molecular profiling of all four cell lines. QSY-21-tagged conjugates were made with all four antibodies, and cell lines were labeled with each solution individually. Cells were then fixed and placed on quartz microscope slides for Raman analysis. Cells were located under the microscope by optical means and aligned with the Raman laser spot. Each analyzed cell was chosen carefully to produce an accurate single-cell profile; no cells that appeared compromised or adhered to other cells were used in the profiling process. Raman spectra were then gathered from a population of fifty cells. Spectra of the nanoparticle solutions were collected at 5pM under the same irradiation conditions as a reference. The rationale centers on the linear nature of Raman signals allowing for a relation between number of particles present and total Raman response. A labeled cell will therefore produce a Raman spectrum with a magnitude proportional to the number of particles bound to the cell surface. The polymer layer that stabilizes each nanoparticle prevents any two particles from closing within 10nm of one another outside the cell, thereby eliminating the need to consider plasmon coupling.

Single-color Raman spectra of each cell line and labeling solution were analyzed by extracting a numerical magnitude at a shift of 1497cm^{-1} (corresponding to the most intense Raman scattering produced by QSY-21) from the cell spectra. To compare the relative magnitude of particle binding between different nanoparticle solutions, the reference spectrum of each antibody-NPC solution was normalized to a standard value of

1,000 counts, and the normalization factor applied to all spectra of cells which were labeled by this solution.

The known expression of each marker is given in Table 5.1. In addition, marker profiling by flow cytometry was conducted on each cell line to verify relative expression for direct comparison. After applying the normalization factor, the relative magnitudes of each marker strongly reflect the expression profiles of each cell line. Figure 5.5 displays the average marker expression as given by single-color Raman analysis.

Table 5.1: Relative Surface Marker Expression by Cell Line

	EpCAM	HER-2	CD44	IGF-1R
SK-BR-3	Positive	Positive	Negative	Negative
MDA-MB-468	Positive	Weak/Negative	Negative	Weak
MCF-7	Positive	Negative	Moderate	Negative
MDA-MB-231	Negative	Negative	Positive	Negative

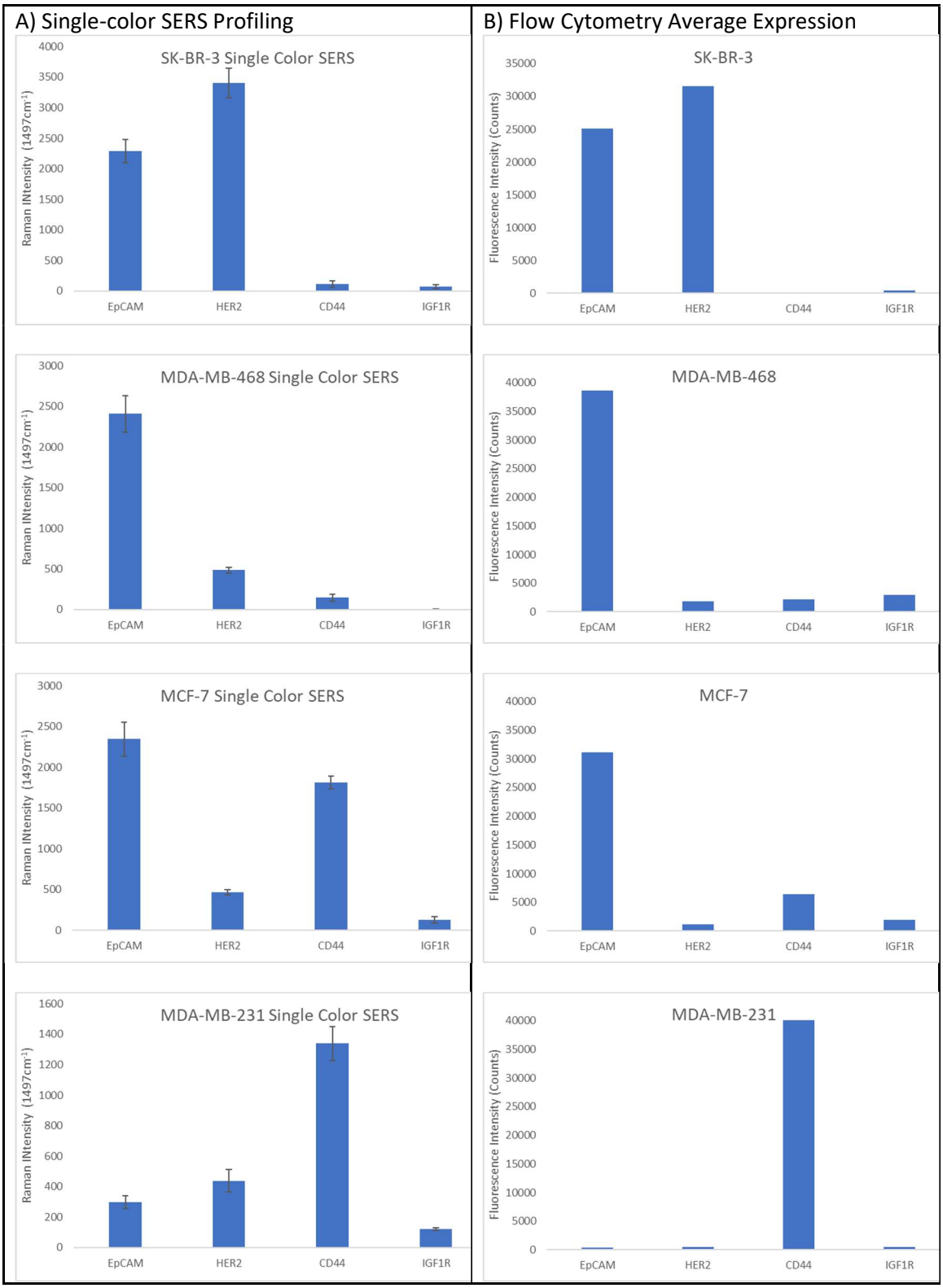

Figure 5.5: A) Average expression of markers on breast cancer cell lines as determined by single-color NPC profiling. B) Average expression of markers on breast cancer cell lines determined by flow cytometry.

The nanoparticle-based profiling correctly identified a greater expression of HER2 in SK-BR-3 cells relative to EpCAM, and both CD44 and IGF-1R responses were indistinguishable from control. MDA-MB-468 showed a strong EpCAM response in accordance with expression measured with flow cytometry and weak response with the other three markers. MDA-MB-231 matched as well, with minimal Raman response measured for all markers except CD44. MCF-7, while classically considered negative for HER2 and weakly positive for CD44, demonstrated similar magnitude of Raman response for both. Flow cytometry confirmed the weak CD44 expression. The results overall reflect the surface marker expressions of each cell line, thereby confirming the plausibility of using IO-Au NPCs as a vehicle for Raman-based molecular profiling.

Molecular Profiling of Cells with Multicolor IO-Au SERS NPCs. Antibody-IO-Au NPC conjugates were produced with each nanoparticle solution labeled with a separate Raman reporter and antibody. 300,000 cells dispersed in PBS were mixed with 10μL of each 50pM NPC solution, incubated, fixed, and mounted on a quartz microscope slide as described before. Raman spectra of individual cells were gathered using the parameters and criteria laid out above. Spectra of all four NPC conjugate solutions were collected as well.

Despite the four dye molecules being chosen for distinct peak separation, the additive nature of combined Raman spectra does not allow for direct measurement of peak maxima as a quantitative measurement while conducting multiplex detection. Therefore, deconvolution of the gathered cell spectra was carried out using a classical least squares (CLS) fitting based on the reference spectra provided by the pure antibody-SERS NPCs. The formula is given below:

1) $$S_{total} = C_1S_1 + C_2S_2 + C_3S_3 + C_4S_4 + \Delta$$

Input was given as a 'pure' spectrum (S) of each contributing source. The software then generated a model for fitting combined spectra into combinations of these four spectra. Cell spectra were inputted (S_{total}) and the program will assign each C a value iteratively until the error factor (Δ) is minimized. These output C factors represent a fraction of the input spectra of each individual contributor.

Detection and Molecular Profiling of Cells with Multicolor IO-Au SERS NPCs in PBS and Whole Blood. Validation of the microfluidic device design in combination with the profiling mechanism was conducted by spiking between 5 and 500 SK-BR-3 cells into 1mL PBS and labeling with 5pM (final concentration) of four-color SERS NPCs. Each sample was introduced into the microfluidic device and pumped through at optimal flow rate in the presence of a magnet, which isolated labeled cells. After flow was complete, the captured sample was washed with PBS (50μL/min for two minutes) and stained with anti-CD45-FiTC and DAPI by flowing each solution in turn across the device at a rate of 50μL/min for five minutes. Cells were then fixed by 4% paraformaldehyde solution, flowed through at 10μL/min for five minutes, and washed once more with PBS, after which was held in the chamber to avoid drying out the cells. Captured, stained cells were observed under bright field and fluorescence microscopy. Morphologically normal cells which were captured in the magnetic chamber, DAPI-positive, and CD45-negative were classified as possible cancer cells and counted for capture efficiency calculation. Finally, each of the cancer cells was interrogated by the Raman microscope to gather SERS spectra of the captured population. The spectra was processed according to the same procedure above. This process is demonstrated in Figure

5.6, in which two SK-BR-3 cells are visualized under bright field, fluorescence, and then interrogated by Raman spectroscopy.

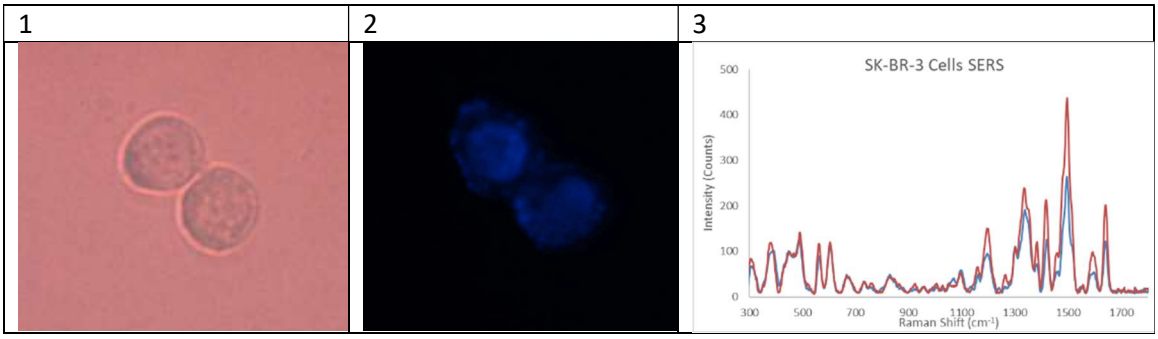

Figure 5.6: SK-BR-3 cells as viewed under the combined Raman/Fluorescence microscope 1) Bright Field image of SK-BR-3 cells, 2) Combined DAPI and CD45-FiTC fluorescence image of the same cells, 3) SERS of the two cells collected.

Capture efficiency was recorded as a fraction of total SERS-active cancer cells captured over total cancer cells spiked into the solution. The capture efficiency varied widely from experiment to experiment, while calculated capture efficiency as performed prior was very consistent. This is likely due to the limitations of locating all captured cells manually in an area that is very large relative to the cells being analyzed. This could be greatly improved with automation of the stage and software that identifies and analyzes cells automatically, such as with the LabSpec 6 ParticleFinder function. Capture specificity was exceptional; from whole blood, the number of cells that were SERS-inactive, DAPI-negative, and/or CD45 positive was minimal. Deconvoluted SERS spectra displayed nearly-identical relative molecular profiles for the captured populations of SK-BR-3 to those gathered previously, showing that conducting cell labeling in the complicated environment of whole blood did not adversely affect cell profiling. Notably, the distributions for larger populations was more in line with known expressions. This may indicate that parent tumor heterogeneity may influence molecular profiling and it may be difficult to make biopsy-accurate determinations on cells captured from patients

with low CTC counts. The time from introduction of blood to the device and commencement of detection was twenty-one minutes, which will increase to approximately 40 minutes when analyzing 7.5mL of blood.

Figure 5.7 graphically displays the C values as produced during the above multicolor profiling experiment. Again, strong agreement in relative abundance of each surface marker is observed. EpCAM magnitude relative to HER2 in SK-BR-3 is lower than that observed in both flow cytometry and the single-color experiments but remains attributable as a positive result. Both MDA-MB-468 and MCF-7 produced EpCAM magnitudes like that of SK-BR-3, further confirming this. Deconvolution of Raman spectra gathered from MDA-MB-231 once again reflects its surface profile of high concentrations of CD44, however disproportionately high contributions of EpCAM and HER-2 labeling appear. Compared to other cell lines which have minimal contribution from nanoparticles seeking non-expressed markers, this appears to be a characteristic exclusive to the MDA-MB-231 cell line. Deconvoluted spectra lose some accuracy due to spectral overlap; this does not appear to modify the identification of highly positive marker expressions. However, weaker expressions such as the low but distinct CD44 presence on MCF-7 cells may prove difficult to distinguish, indeed the contribution of CD44-targeted NPC spectra are nearly identical between MDA-MB-468 and MDA-MB-231. Finally, the over-detection of other markers on MDA-MB-231 may indicate that this strategy may have difficulties in proper profiling of circulating cancer stem cells.

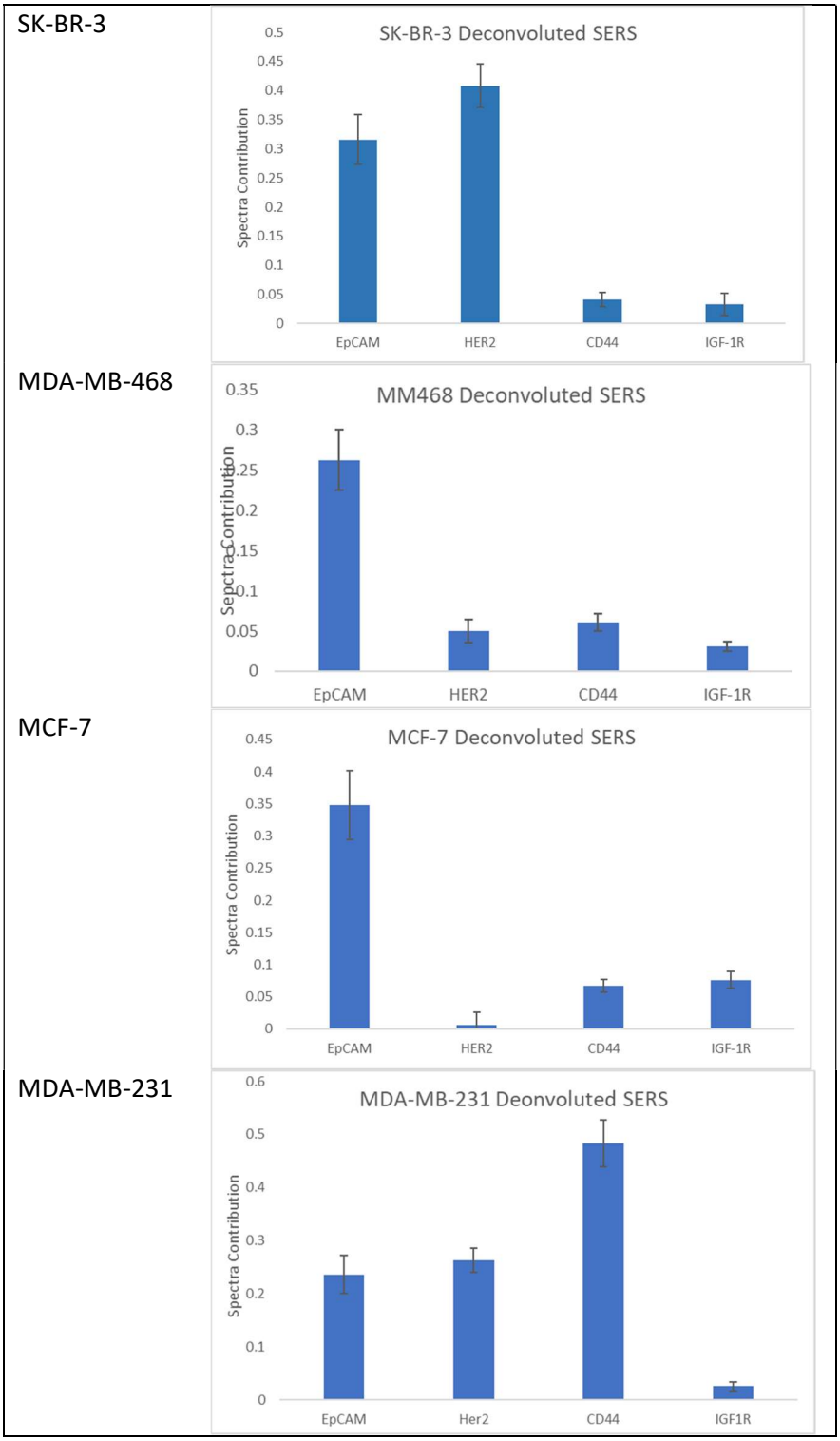

Figure 5.7: Average 'C' values (spectral contribution) of deconvoluted spectra of 50 cells isolated from PBS by magnetic separation on the microfluidic device.

Conclusion

We have developed an on-line simple assay that utilizes dual-function magnetic-optical nanoparticles to simultaneously isolate and enrich target cells prior to interrogation with a Raman instrument to display, which allows for sensitive multiplexed molecular profiling of biomarkers. This development directly answers the request in Bhana *et al.* to incorporate a multiplexed marker detection system while also providing a platform to evaluate individual cells and selectively eliminate false positives from immune cells or cell debris. This system is currently being used to assay blood samples to demonstrate clinical utility. Due to the fingerprint signatures of Raman spectra and the adaptability of antibody conjugation, the system can be expanded to fit many more marker-Raman dye pairs for considerable multiplexed molecular profiling. Therefore, in the future, a wider array of marker-dye pairs should be synthesized, verified, and incorporated into the multicolor cocktail to expand detection capability. Of particular interest is a more diverse choice of markers to capture and detect a wider range of cancer types, or to target surface markers that provide clinically-relevant details of cancer status.

The assay could be translated to the clinical setting with ease and could potentially demonstrate considerable utility. The simple and rapid isolation process coupled with the addition of automation to the cell location process and integrated software would allow for expedient patient blood sampling which could yield detailed information about patient prognosis during treatment and better inform doctors at the point of care. The continued development of this system has considerable potential impact on the treatment of cancer.

Chapter 6

Conclusions and Future Outlook

The work in this dissertation has focused on the development of two major areas in cancer medicine. In Chapter 4, we developed a gold nanorod-based complex for the purpose of conducting combined photothermal and photodynamic therapy. In Chapter 5, we developed a rapid system to capture, detect, and profile the surface markers of mimic circulating tumor cells spiked into PBS and whole blood. Chapter 3 explores the development of a new antibody conjugation method which is both cooperative with the group's recent synthetic developments and improves the effectiveness of SERS-active bioconjugated nanoparticles.

Chapter 3 discusses the rationale behind developing a new protein conjugation method for the purposes of creating nanoparticles which require a minimal number of purification steps to improve SERS activity. The strategy involved the use of carbodiimide linking between protein and a polyethylene glycol-thiol linking molecule, which could then be bound to the nanoparticle in one reaction. Initially, horseradish peroxidase was used as a model to narrow down the synthetic parameters using colorimetric TMB assay to determine conjugation success. Optimized conditions were then transferred to antibody conjugation of gold nanoparticles, which was verified by nanoparticle labeling of cells and imaged under dark field microscopy. The selectivity was explored using multiple cell lines with varying surface marker expressions. Future exploration may narrow down unexplored parameters and yield further control of the conjugation process used by our group for a wide range of experiments not limited to those discussed previously. This includes the continued conjugation of gold nanoparticles

for immunotargeting and SERS detection of CTCs and exosomes. Recently, the carbodiimide procedure laid out by the work described in Chapter 3 was used for gold surface modification for SERS-based exosome detection[106], and other group members are applying antibody-conjugated gold nanoparticles to CTCs captured on a size-based separation chip. Together these projects demonstrate the utility of this method for future work.

Chapter 4 discusses the development of NIR-absorbing gold nanorods electrostatically coated with SiNC photosensitizer and stabilized with an alkylthiol-PEG made from three different alkyl lengths. These nanocomplexes demonstrated exceptional stability in physiological media with a release of no more than 8% of SiNC payload over 7 hours, while demonstrating greatly heightened release of up to 90% in the presence of cells. Laser irradiation experiments proved the complex's ability to induce cell death by photothermal and photodynamic means. In comparison to PDT and PTT methods individually, statistical analysis of the combined therapy indicates the potential of a synergistic effect in which the nanocomplex generates greater percentage of cell death than the hypothetical application of PDT and PTT individually on the same population. Future expansion of this PDT/PTT nanocomplex involves the introduction of a targeting strategy, such as antibody conjugation. This targeted nanocomplex, if developed, could be implemented in an animal study to demonstrate its value as a viable treatment function. Ultimately, this treatment strategy could provide a strong non-invasive treatment option which is, in a singular application, more effective than the two treatment options it combines.

Chapter 5 discusses the development of a one-device assay for the capture, detection, and multiplexed molecular profiling of mimic circulating tumor cells in PBS and whole blood. Iron oxide-gold core-shell nanopopcorn were labeled with four Raman-active dye and conjugated with antibodies targeting four different cancer cell surface markers. These nanoparticles were used to label and profile cancer cell lines in suspension, then to capture the cells on a newly-designed microfluidic device under a magnetic field. Cells were then interrogated by an integrated fluorescence and Raman microscope. The Raman spectra were deconvoluted by classical least squares regression to determine the proportional amount of each surface marker tagged with a nanoparticle on individual cells. The result is a molecular profile of captured cells. With an optimal flow rate of 200μL/min, blood samples can be processed quickly and efficiently without the need for multiple preparatory steps or separations. If combined with automated cell-finding software and an automatic stage, the profiling of all captured cells could be sped up considerably, thereby providing an optimized platform for clinical use as close to the point of care as possible. Additionally, this study demonstrates the use of four marker-dye pairs, which can be greatly expanded to more than twice as many targets in future studies. Such an assay which could provide a new capability to rapidly acquire extensive molecular profiling of CTCs near the point of care. This could provide doctors with prognostic information, potential treatment vectors, feedback on treatment efficacy, and ultimately improve the quality of information present for critical decisions.

References

1) Dreaden, E. C.; Alkilany, A. M.; Huang, X.; Murphy, C. J.; El-Sayed, M. A. "The Golden Age: Gold Nanoparticles for Biomedicine." *Chem. Soc. Rev.* **2012**, *41*, 2740–2779.

2) S. Chaturvedi and P. N. Dave, "Emerging Applications of Nanoscience", *Materials Science Forum*, **2014** *781*, 25-32

3) Eustis, S.; El-Sayed, M. A. "Why Gold Nanoparticles Are More Precious than Pretty Gold: Noble Metal Surface Plasmon Resonance and Its Enhancement of the Radiative and Nonradiative Properties of Nanocrystals of Different Shapes." *Chem. Soc. Rev.* **2006**, *35*, 209–217.

4) Mobasser, S. and Ali Akbar Firoozi. "Review of Nanotechnology Applications in Science and Engineering" *J. Civ. Eng. Urb.* **2016**, *6(4)* 84-93

5) Haruta, M., M. Date. "Advances in the Catalysis of Au Nanoparticles" *Appl. Cata. A.* **2001** *222* 427

6) Hashmi, A. S. K. and G. J. Hutchings. "Gold Catalysis" *Angew. Chem. Int. Ed.* **2006** *45* 7896

7) Jin, Y.; Jia, C.; Huang, S.; O'Donnell, M.; Gao, X. Multifunctional Nanoparticles as Coupled Contrast Agents. *Nat. Commun*. **2010**, *1*, 41

8) Saini, R.; Saini, S. and Sugandha Sharma. "Nanotechnology: The Future Medicine" *J Cutan Aesthet Surg*. **2010** *3(1)*: 32–33.

9) Pankhurst, Q. A.; Connolly, J.; Jones, S. K.; Dobson, J. Applications of Magnetic Nanoparticles in Biomedicine. *Journal of Physics D: Applied Physics*, **2003**, *36*, 167–181.

10) Pankhurst, Q. A., J Connolly, S K Jones, J. Dobson "Applications of Magnetic Nanoparticles in Medicine" *Journal of Physics D: Applied Physics* **2003**, *36*, 167.

11) American Cancer Society. Cancer Facts and Figures 2015 https://www.cancer.org/research/cancer-facts-statistics/all-cancer-facts-figures/cancer-facts-figures-2015.html (accessed 2 Jun 2018)

12) Faraday, M. *Philos. Trans.* **1857**, *147* 145

13) Turkevich, J., Stevenson, P. C., and J. Hillier. "The Formation of Colloidal Gold" *Discuss. Faraday Soc.* **1951,** *11,* 55.

14) Turkevich, J. "Colloidal Gold" *Gold Bull.* **1985***, 18,* 86

15) Frens, G. *Nature: Phys. Sci.* **1973,** *241,* 20

16) Boon-Kin Pong, Hendry I. Elim, Jian-Xiong Chong, Wei Ji, Bernhardt L. Trout,,⊥ and Jim-Yang Lee. "New Insights on the Nanoparticle Growth Mechanism in the Citrate Reduction of Gold(III) Salt: Formation of the Au Nanowire Intermediate and Its Nonlinear Optical Properties" *J. Phys. Chem. C* **2007***, 111*, 6281-6287

17) Chow, M. K.; Zukoski, C. F. *J. Colloid Interface Sci.* **1994***, 165*, 97

18) Brust, M., Walker, M. Bethell, D. Schriffin, D. J., and R. J. Whyman. *J Chem Soc Chem Commun.* **1994** *801*.

19) Hostetler, M. J.; Green, S. J.; Stokes, J. J.; Murray, R. W. *J. Am. Chem. Soc.* **1996***, 118*, 4212

20) Templeton, A. C.; Hostetler, M. J.; Kraft, C. T.; Murray, R. W. *J. Am. Chem. Soc.* **1998***, 120*, 1906

21) Zou, M., Li, J., Zhang F., and Y. Jin. "Ultrasonic Synthesis of Gold Nanoparticles and Its Use in Immunochromatographic Assay for Detection of Kanamycin" *Analytical Letters,* **2010** *43:5*, 867-875,

22) Schmid G., Pfeil R., Boese R., Bandermann F., Meyer S., Calis G.H.M., and J. W. A. van der Velden *Chem Ber.* **1981** *114,* 3634–3642.

23) Brown, K.R. Fox, A. P. and J. M. Natan *J. Am. Chem. Soc.* **1996** *118,* 1154

24) Pyrpassopolous, S., Niarchos, D., Nounesis, G., Boukis, Zafiropuolou, I., and V. Tzitzios. *Nanotechnology* **2007** *18(28),* 285602

25) Moon, S. Y., Kusunose, T., and T. Sekino. *Mater. Lett.* **2009** *63,* 2038

26) Zhao, P. Li, N. and Didier Astruc. "State of the Art in Gold Nanoparticle Synthesis" *Coord. Chem. Rev.* **2013** *257* 638-665

27) Jana N. R., Gearheart L, Murphy C. *J. Adv Mater.* **2001** *13(18),* 1389 – 1393

28) Wang Z. L., Mohamed M. B., Link S., El-Sayed M. A. *Surf Sci.* **1999** *440*, 809–814.

29) Nikoobakht B, El-Sayed MA. *Langmuir.* **2001** *17*, 6368–6374.

30) Sau TK, Murphy CJ. *Langmuir.* **2004** *20,* 6414–6420.

31) Perez-Juste, J. Liz-Marzan, L. M., Carnie, S., Chan, D. Y. C., and P. Mulvaney. *Adv. Funct. Mater.* **2004** *101,* 571

32) Grzelczak, M., Pe´rez-Juste, J., Mulvaney, P., and L. M. Liz-Marza. Shape control in gold nanoparticle synthesis *Chem. Soc. Rev.* **2008** *37*, 1783–1791

33) Nikoobakht, B. El-Sayed, M. A. *Chem Mater.* **2003** *15,* 1957

34) Yang, X., Yang, M. Pang, Bo., Vara, M. and Y. Xia. "Gold Nanomaterials at Work in Biomedicine" *Chem. Rev.* **2015** *115*, 10410−10488

35) Bohren, C. F.; Huffman, D. R. *Absorption and Scattering of Light by Small*

Particles Wiley-VCH, Veinheim, Germany. 1998

36) Huang, X. Jain, P. K., El-Sayed, I. H. El-Sayed, M. A. *Lasers Med. Sci.* **2008** *23*, 217.

37) Bardhan, R., Lal S., Joshi, A., and Naomi J. Halas. "Theranostic Nanoshells: From Probe Design to Imaging and Treatment of Cancer" *Accts. Chem. Res.* **2011** *44 (10),* 936-946

38) Bardhan, R.; Grady, N. K.; Cole, J.; Joshi, A.; Halas, N. J. "Fluorescence enhancement by Au nanostructures: Nanoshells and nanorods." *ACS Nano* **2009** *3*, 744–752

39) Bardhan, R.; Grady, N. K.; Halas, N. J. "Nanoscale control of near-infrared fluorescence enhancement using Au nanoshells." *Small* **2008** *4*, 1716–1722

40) Kneipp, K.; Kneipp, H.; Itzkan, I.; Dasari, R. R.; Feld, M. S. "Surface-Enhanced Raman Scattering and Biophysics." *J. Phys. Condens. Matter* **2002** *14*, R597– R624

41) Schatz, G. C.; Young, M. A.; Van Duyne, R. P. "Electromagnetic Mechanism of SERS." *Top. Appl. Phys.* **2006**, *103*, 19–46.

42) Nie, S. and Steven R. Emory. "Probing Single Molecules and Single Nanoparticles by Surface-Enhanced Raman Scattering" *Science* **1997** *275,* 1102-1106

43) Kneipp, K.; Wang, Y.; Kneipp, H.; Perelman, L.; Itzkan, I.; Dasari, R.; Feld, M. "Single Molecule Detection Using Surface-Enhanced Raman Scattering (SERS)." *Phys. Rev. Lett.* **1997** *78*, 1667–1670.

44) Sau, T. K.; Rogach, A. L.; Jäckel, F.; Klar, T. A.; Feldmann, J. "Properties and Applications of Colloidal Nonspherical Noble Metal Nanoparticles." *Adv. Mater.* **2010** *22*, 1805–1825

45) Chanduri, R. G. and Santanu Paria. “Core/shell Nanoparticles: Classes, Properties, Synthesis Mechanisms, Characterization, and Applications” *Chem. Rev.* ***2012*** *112*, 2373-2433

46) Tarin, C., Carrill, M., Martin-Ventura, J. L. Markuerkiaga, Irati., Padro, D., Llamas-Granda, P., Moreno, J. A., Garcia, I., Genicio, N., Plaza-Garcia, S., Blanco-Colio, L. M., Penades, S. and Jesus Egido. “Targeted Gold-coated Iron Oxide Nanoparticles for CD163 Detection in Atherosclerosis by MRI” *Sci. Rep.* ***2015*** *5* 17135

47) Tiwari P. M., Vig K, Dennis VA, Singh SR. Functionalized Gold Nanoparticles and Their Biomedical Applications. Nanomaterials. 2011;1(1):31-63.

48) Jazayeri, M. H. Amani, H., Pourfatollah, A. A, Pazoki-Toroudi, H., and Bijan Sedighimoghaddam. “Various Methods of Gold Nanoparticle Conjugation to Antibodies” *Sensing and Bio-Sensing Research* **2016** *9* 17–22

49) I.H. El-Sayed, X. Huang, M.A. El-Sayed “Surface plasmon resonance scattering and absorption of anti-EGFR antibody conjugated gold nanoparticles in cancer diagnostics: applications in oral cancer” *Nano Lett.* ***2005*** *5 (5)*, 829-834

50) Z. Zhang, S. Wang, H. Xu, B. Wang, C. Yao “Role of 5-aminolevulinic acid-conjugated gold nanoparticles for photodynamic therapy of cancer” *J. Biomed. Opt.* **2015** *20 (5)* 51043

51) S. Kumar, J. Aaron, K. Sokolov “Directional conjugation of antibodies to nanoparticles for synthesis of multiplexed optical contrast agents with both delivery and targeting moieties” *Nat. Protoc.* **2008** *3(2),* 314-320

52) R.-A. Sperling, W. Parak "Surface modification, functionalization and bioconjugation of colloidal inorganic nanoparticles" *Philos. Trans. R. Soc. Lond. A Math. Phys. Eng. Sci.* **2010** *368 (1915)* 1333-1383

53) G. Hermanson. *Bioconjugate Techniques (second ed.)*, Academic Press, London, UK. **2008**

54) Beck, A., Goetsch, L., Dumontet C., and Nathalie Corvaïa *Nature Rev. Drug Discovery* **2017** *16,* 315–337

55) Tran, S., DeGiovanni, P. J., Piel, B., and Prakash Rai. "Cancer Nanomedicine: A Review of Recent Success in Drug Delivery." *Clinical and Translational Medicine* **2017** *6,* 44

56) Mody, V.V., Cox, A., Shah, S. "Magnetic nanoparticle drug delivery systems for targeting tumor" *Appl Nanosci* **2014** *4* 385

57) Huschka, R., Zuloaga, J., Knight, M. W., Brown, L. V., Nordlander, P., and Naomi Halas. "Light-induced Release of DNA from Gold Nanoparticles: Nanoshells and Nanorods" *J. Am. Chem. Soc.* **2011** *133,* 12247-12255

58) Ren, F. Bhana, S., Norman, D. Johnson, J. Xu, L., Baker,D. L., Parrill, A. L. and X. Huang. "Gold nanorods carrying paclitaxel for photothermal-chemotherapy of cancer." *Bioconjugate Chem.* **2013** *24*, 376-386.

59) Nakamura, Y., Mochida, A., Choyke, P. L., and H. Kobayashi. "Nanodrug Delivery: Is the Enhanced Permeability and Retention Effect Sufficient for Curing Cancer?" *Bioconjugate Chem.,* **2016***, 27(10)*, 2225–2238

60) Wu, M. and Shengwu Huang. "Magnetic nanoparticles in cancer diagnosis, drug delivery and treatment" *Mol Clin Oncol.* **2017** *7(5)*, 738–746.

61) Hong, E. J., Choi, D. G. and M. S. Shim. “Targeted and Effective Photodynamic Therapy for Cancer using Functionalized Materials” *Acta Pharmaceutica Sinica B.* **2016** *6(4)*, 297-307

62) T. J. Dougherty, C. J. Gomer, B. W. Henderson, “Photodynamic Therapy” *J. Nat. Cancer Institute* **1998**, *90*, 889

63) D. E. Dolmans, D. Fukumura, R. K. Jain, “Photodynamic Therapy for Cancer” *Nat. Rev. Cancer **2003** 3*, 380

64) J. P. Celli, B. Q. Spring, I. Rizvi, C. L. Evans, K. S. Samkoe, S. Verma, B. W. Pogue, T. Hasan, “Imaging and Photodynamic Therapy: Mechanisms, Monitoring, and Optimization” *Chem. Rev.* **2010**, *110*, 2795.

65) Zhang, L. Gao S, Zhang F, Yang K, Ma Q, Zhu L. “Activatable hyaluronic acid nanoparticle as a theranostic agent for optical/photoacoustic image-guided photothermal therapy.” *ACS Nano* **2014** *8*, 12250–12258

66) Gui, C. and Cui D. “Functionalized Gold Nanorods for Tumor Imaging and Targeted Therapy.” *Cancer Biol Med* **2012** *9(4)* 221-233

67) Mendes, R., Pedrosa, P., Lima, J. C., Fernandes, A. R., P. V. Baptista. “Photothermal Enhancement of Chemotherapy in Breast Cancer by Visible Irradiation of Gold Nanoparticles” *Sci. Rep.* **2017** *7,* 10872

68) Ali, M. R. K., Rahman, M. A., Wu, Y., Han, T., Peng, X., Mackey, M. A., Wang, D., Shin, H. J., Chen, Z. G., Xiao, H., Wu, R., Tang, Y., Shin, D. M. and M. A. El-Sayed. “Efficacy, Long-term Toxicity, and Mechanistic Studies of Gold Nanorods Photothermal Therapy of Cancer in Xenograft Mice” *PNAS* **2017** 3110-3118

69) Brock G, Castellanos-Rizaldos E., Hu L., Coticchia C., Skog J. "Liquid biopsy for cancer screening, patient stratification and monitoring." *Transl. Cancer Res.* **2015** *4* 280-290.

70) Diaz Jr LA, Bardelli A. "Liquid biopsies: genotyping circulating tumor DNA." *J Clin Oncol* **2014**; *32* 579-86.

71) Diehl F, Schmidt K., Choti MA. "Circulating mutant DNA to assess tumor dynamics." *Nat Med* **2008** *14*, 985-90.

72) Rissin DM, Kan, CW, Campbell T. G. "Single-molecule enzyme-linked immunosorbent assay detects serum proteins at subfemtomolar concentrations." *Nat Biotechnol.* **2010** *28*, 595-9.

73) Rosi NL, Mirkin CA. "Nanostructures in Biodiagnostics." *Chem Rev* **2005** *105*, 1547-56.

74) Lo Cicero A, Stahl PD, Raposo G. "Extracellular vesicles shuffling intercellular messages: for good or for bad." *Curr Opin Cell Biol* **2015** *35*, 69-77

75) Liberko M, Kolostova K, Bobek V. Essentials of circulating tumor cells for clinical research and practice. *Crit Rev Oncol Hematol* **2013** *88* 338-56.

76) Valastyan S, Weinberg RA. "Tumor metastasis: molecular insights and evolving paradigms." *Cell* **2011** *147*, 275-92.

77) Hüsemann Y, Geigl J. B., Schubert F. "Systemic spread is an early step in breast cancer." *Cancer Cell* **2008** *13*, 58-68.

78) Miller M. C., Doyle G. V., Terstappen L. W. M. M. "Significance of circulating tumor cells detected by the CellSearch systemin patients with metastatic breast colorectal and prostate cancer." *J Oncol* **2010** *2010* 617421.

79) Mocellin S, Hoon D, Ambrosi A, Nitti D, Rossi CR. "The prognostic value of circulating tumor cells in patients with melanoma: a systematic review and meta-analysis." *Clin Cancer Res* **2006** *12* 4605-4613.

80) Hiltermann TJN, Pore MM, van den Berg A, *et al.*. "Circulating tumor cells in small-cell lung cancer: A predictive and prognostic factor." *Ann Oncol* **2012** *23*, 2937-42.

81) Hunter KW, Crawford NP, Alsarraj J. "Mechanisms of metastasis." *Breast Cancer Research* **2008** *10*

82) Arya SK, Lim B, Rahman ARA. Enrichment, detection and clinical significance of circulating tumor cells. *Lab Chip* **2013** *13*, 1995-2027.

83) Huang, X., O'Connor, R. T., Kwizera, E. A. "Gold Nanoparticle-based Platforms for Circulating Cancer Marker Detection" *Nanotheranostics* **2017** *1*(1), 80-102

84) Liberti P. A., Rao C. G., Terstappen L. W. M. M. "Optimization of ferrofluids and protocols for the enrichment of breast tumor cells in blood." *J Magn Magn Mater* **2001** *225,* 301-7.

85) Sheng W, Chen T, Tan W, Fan ZH. "Multivalent DNA nanospheres for enhanced capture of cancer cells in microfluidic devices." *ACS Nano* **2013** 7, 7067-7076

86) Costa MM, Escosura-Muñiz A, Nogués C, Barrios L, Ibáñez E, A Merkoçi. "Simple monitoring of cancer cells using nanoparticles." *Nano Lett.* **2012** *12*, 4164-71.

87) Costa MM, Escosura-Muñiz A, Nogués C, Barrios L, Ibáñez E, MerkoçI A. "Detection of circulating cancer cells using electrocatalytic gold nanoparticles." *Small* **2012** *8,* 3605-3612

88) Jung S. Y., Ahn S., Seo E., Lee S. J. "Detection of circulating tumor cells via an X-ray imaging technique." *J Synchrotron Rad* **2013** *20,* 324-31

89) Sha M. Y., Xu H. X., Natan M. J., Cromer R. “Surface-enhanced Raman scattering tags for rapid and homogeneous detection of circulating tumor cells in the presence of human whole blood.” *J Am Chem Soc* **2008** *130*, 17214-5

90) Shi W., Paproski R. J., Moore R., Zemp R. “Detection of circulating tumor cells using targeted surface-enhanced Raman scattering nanoparticles and magnetic enrichment.” *J Biomed Optics* **2014** *19,* 056014

91) Wang X., Qian X. M., Beitler J. J., Chen Z. G., Khuri F. R., Lewis M. M., Shin H. J. C., Nie S. M., Shin D. M. “Detection of circulating tumor cells in human peripheral blood using surface-enhanced Raman scattering nanoparticles.” *Cancer Res* **2011** *71*, 1526-32.

92) Bhana S., Chaffin E., Wang Y., Mishra S. R., Huang X. “Capture and detection of cancer cells in whole blood with magnetic-optical nanoovals.” *Nanomedicine (Lond)* **2014** *9*, 593-606.

93) Nima ZA, Mahmood M, Xu Y “Circulating tumor cell identification by functionalized silver-gold nanorods with multicolor, super-enhanced SERS and photothermal resonances.” *Sci Rep* **2014** *4*, 4752.

94) Kwizera, E. A.; Chaffin, E.; Shen, X.; Chen, J.; Zou, Q.; Wu, Z.; Gai, Z.; Bhana, S.; O’Connor, R. T.; Wang, L.; Adhikari, H.; Mishra, S.; Wang, Y.; and X. Huang. “Size- and Shape-Controlled Synthesis and Properties of Magnetic-Plasmonic Core-Shell Nanoparticles.” *J. Phys. Chem. C* **2016**, *120*, 10530-10546

95) Josephy, P. D., Eling, T., and R. P. Mason. “The Horseradish Peroxidase-catalyzed Oxidation of 3,5,3’,5’-Tetramethylbenzidine” *J. Biol. Chem.* **1982** *257(7)* 3669-3675

96) Huang, X. Peng, X. Wang, Y. Wang, X. Shin, D. M., El-Sayed, M. A. and S. Nie. "A reexamination of active and passive tumor targeting by using rod-shaped gold nanocrystals and covalently conjugated peptide ligands." *ACS Nano* **2010** *4*, 5887

97) Kuo, W. S., Chang, C. N. Chang, Y. T. Yang, M. H., Chien, Y. H., Chen, S. J., C. S. Yeh, "Gold nanorods in photodynamic therapy, as hyperthermia agents, and in near-infrared optical imaging." *Angew. Chem. Int. Ed* **2010** *49*, 2711

98) Jang B., Park J. Y., Tung C. H., Kim I. H., and Y. Choi "Gold nanorod-photosensitizer complex for near-infrared fluorescence imaging and photodynamic/photothermal therapy in vivo." *ACS Nano.* **2011** *5(2)* 1086-1094.

99) Kim J. Y., Choi W. I., Kim M., Tae G. "Tumor-targeting nanogel that can function independently for both photodynamic and photothermal therapy and its synergy from the procedure of PDT followed by PTT." *J Control Release.* **2013** *171(2)*, 113-121

100) Kuo W.S., Chang Y.T., Cho K.C., Chiu K.C., Lien C.H., Yeh C.S., and S. J. Chen. "Gold nanomaterials conjugated with indocyanine green for dual-modality photodynamic and photothermal therapy." *Biomaterials.* **2012** *33(11)* 3270-3278

101) Hauck, T. S., Jennings, T. L., Yatsenko T., Kumaradas J. C, and W. C. W. Chan. "Enhancing the Toxicity of Cancer Chemotherapeutics with Gold Nanorod Hyperthermia" *Adv. Mater.* **2008** *20*, 3832.

102) Maheswaran, S., Haber, D. A. "Circulating Tumor Cells: A Window into Cancer Biology and Metastasis" *Int. J Oncol* **2009** *34(4)* 881-895.

103) Danova, M., Torchio, M., and G. Mazzini. "Isolation of Rare Circulating Tumor Cells in Cancer Patients: Technical Aspects and Clinical Implications" *Expert Rev. Mol. Diagn.* **2011** *11*. 473-485

104) Goon, I. Y.; Lai, L. M. H.; Lim, M.; Munroe, P.; Gooding, J. J.; Amal, R. “Fabrication and Dispersion of Gold-Shell-Protected Magnetite Nanoparticles: Systematic Control Using Polyethyleneimine.” *Chem. Mater.* **2009**, *21*, 673–681

105) Salomon D. S., Brandt R., Ciardiello F., and N. Normanno. “Epidermal growth factor-related peptides and their receptors in human malignancies.” *Crit Rev Oncol Hematol.* **1995** *19(3)* 183-232

106) Kwizera, E. A., O’Connor, R. T., Vinduska, V., Williams, M., Butch, E. R., Snyder, S. E., Chen, X., and X. Huang. “Molecular Detection and Analysis of Exosomes using Surface-Enhanced Raman Scattering Gold Nanorods and a Miniaturized Device.” *Theranostics* **2018** *8(10)* 2722-2738